



Large-scale wave impact of a boiling liquid

Rodrigo Ezeta¹ , Bernardo Palacios Muñiz² , Yee Li (Ellis) Fan² ,
Nayoung Kim² , Nicolas Couty³ , Laurent Brosset³  and
Devaraj van der Meer² 

¹Research and Development Department, Maritime Research Institute Netherlands (MARIN), Wageningen, The Netherlands

²Physics of Fluids Group, Max Planck Center Twente for Complex Fluid Dynamics, University of Twente, 7500 AE Enschede, The Netherlands

³Liquid Motions Department, Gaztransport & Technigaz (GTT), Saint-Rémy-lès-Chevreuse, France

Corresponding authors: Rodrigo Ezeta, r.ezeta@marin.nl; Devaraj van der Meer, d.vandermeer@utwente.nl

(Received 15 October 2024; revised 20 December 2024; accepted 20 January 2025)

Wave impact on solid structures is a well-studied phenomenon, but almost exclusively for the case that the impacting liquid (e.g. water) is surrounded by a non-condensable gas (such as air). In this study we turn to wave impact in a boiling liquid, a liquid that is in thermal equilibrium with its own vapour, which is of key relevance to the transport of cryogenic liquids, such as liquified natural gas and liquid hydrogen in the near future. More specifically, we use the Atmosphere facility at MARIN, NL, to prepare water/water vapour systems at different temperatures along the vapour curve. Here, we perform wave impact experiments by generating a soliton in a flume contained within the autoclave of the facility. A bathymetry profile interacts with the soliton, leading to a breaking wave that impacts onto a vertical wall, where we measure the pressures occurring during impact by means of 100 embedded pressure sensors. In boiling liquids, we report wave impact pressures that are up to two orders of magnitude larger than those measured in comparable water–air experiments. We trace these pressures back to the collapse of the entrapped vapour pocket, which we semi-quantitatively describe using a simplified hemicylindrical vapour bubble model, which is in good agreement with the experimental findings. Finally, this allows us to predict the relevance of our findings for the transport of cryogenic liquids in huge overseas carriers where wave impact due to sloshing is the dominant cause of hydrodynamic load of containment systems in cargo tanks.

Key words: condensation/evaporation, wave-structure interactions, bubble dynamics

1. Introduction

Liquid–solid impact is an ubiquitous and often awe-inspiring phenomenon, which is frequently observed in nature, e.g. when ocean waves crash against a harbour quay (Peregrine 2003), a stone lands in a lake (Truscott *et al.* 2014) or seabirds catch their prey (Chang *et al.* 2016). Similar phenomena can be seen during the operation of ocean vessels, connected to hull slamming (Abrate 2013), (re-)entry of a ship into water (Kapsenberg 2011), the landing of sea planes or spacecraft (Seddon & Moatamedi 2006), wet-deck slamming in ships or off-shore structures (Smith *et al.* 1998; Faltinsen 2000; Faltinsen *et al.* 2004), or sloshing (Faltinsen & Timokha 2009). The pressures that are generated during wave impact are often large and short lived, and may have severe detrimental effects on the stability of the structures impacted upon.

One of the key examples of sloshing is found in the huge containers of liquid natural gas (LNG) carriers, where almost the entire load experienced by the structure is connected to sloshing wave impact (Bogaert *et al.* 2010; Dias & Ghidaglia 2018). Although at first sight the above example looks similar to all of those mentioned previously, there is one crucial difference: whereas all previously mentioned examples deal with impact of a liquid (water) surrounded by a non-condensable gas (air), in LNG carriers we are dealing with a liquid (LNG) that is kept at its boiling point, in thermal equilibrium with its own vapour. For brevity, we will refer to this situation as a boiling liquid. This immediately raises the fundamental question of whether phase change may influence the behaviour of the boiling liquid during wave impact.

Since such a system is on, or at least very close to, the vapour curve, even small changes in temperature or pressure may cause condensation or evaporation, which in turn may change the usually mitigating response of the intermediate phase, in this case the vapour. Here, we refer to intermediate phase as the fluid in between water and the solid structure. When this surrounding phase is air, the intermediate phase may have a very non-trivial influence on the generated load, and its distribution on the solid structure (Bogaert *et al.* 2010; Dias & Ghidaglia 2018). One way this may occur is through aeration of the liquid phase (Bredmose *et al.* 2015; Ma *et al.* 2016), but more often, the gas that is trapped in between the liquid and the solid affects the shape of the liquid surface (Hicks *et al.* 2012), and also plays a crucial role in affecting the loading on the solid phase (Hattori *et al.* 1994; Peregrine & Thais 1996; Wood *et al.* 2000; Ermanyuk & Ohkusu 2005; Bredmose *et al.* 2009).

This immediately raises the question of what will happen to this intermediate phase in the case of impact of a boiling liquid in the presence of vapour bubbles (Plesset & Prosperetti 1977; Prosperetti 2017). Or more precisely, under what conditions will condensation occur and possibly cause violent collapse of vapour cavities inside the liquid, that may in turn cause damage to the structure, similar to the many studies of cavitation at, e.g. naval propellers (Brennen 2013; Peters *et al.* 2018; Reuter *et al.* 2022). This is what we investigate in the current work, where water–water vapour systems are created in the unique Atmosphere (ATM) facility at MARIN for several different temperatures on the vapour curve, and in which we will create large-scale wave impacts on a vertical wall instrumented with pressure sensors. Subsequently, we explain our findings with a simplified model that makes use of the Rayleigh–Plesset equation (Brennen 2013), the Plesset–Zwick solution of the convective heat equation (Plesset & Zwick 1952) and an energy–mass balance equation at the liquid–vapour interface allowing for phase change. Aside from a few explorative numerical studies on model systems (Calderón-Sánchez *et al.* 2018; Braeunig *et al.* 2010; Ancellin *et al.* 2012), to date no one has investigated the role of phase change in a boiling liquid in a controlled experiment.

This work is structured as follows. In § 2 we give a brief review of the experimental setup, the ATM facility at MARIN, followed by a short description of how breaking waves are created in the flume. Subsequently, we discuss the experimental results in § 3 where, as an example, a wave impact under boiling liquid conditions at low temperature is compared with a similar impact in air, showing enormous differences in the behaviour of the entrapped vapour or air pocket. This is followed by a discussion of the characteristic pressures occurring during wave impact as a function of wave shape and temperature, exploring the full parameter range studied in this work. In § 4 we present a simplified theoretical model for the vapour pocket dynamics based on the two-dimensional Rayleigh–Plesset equation, which is subsequently compared with experimental findings and written in dimensionless form to show that the observed phenomena are essentially governed by a single dimensionless parameter. The work is concluded in § 5.

2. Experimental setup

The experiments were carried out in the ATM facility located in MARIN. This new large-scale facility consists of a cylindrical autoclave (2.5 m in diameter and 15 m in length), shown in figure 1(a), in which we can control and monitor independently the ambient pressure p_0 from 0.02 to 10 bar, the liquid (water) and gas temperature T_0 from 15 to 200 °C and the gas composition to any mixture of non-condensable gases (e.g. He, N₂, Ar) and condensable gases (water vapour). For the purpose of this work, especially the latter feature is used, creating – at any desired, physically attainable temperature – an atmosphere of water vapour in equilibrium with the liquid (water) that is contained in a horizontal flume (12 m in length, 0.60 m in width) positioned inside of the autoclave with a piston-type wavemaker. (Although the thermodynamics of a liquid and its vapour in thermal equilibrium is considered textbook knowledge, we provide the vapour curve of water with the temperature set points used in – and some essential relations needed for – the current work in Appendix C.) The instrumentation of the ATM includes an encoder that measures the position of the wavemaker in time, three wave gauges (provided by three Manta G235-B cameras) at various positions along the flume to extract the wave elevation and monitor the travelling wave shape, two Photron SAX high-speed cameras located near a vertical wall opposite to the wavemaker (the so-called impact wall), several pressure and temperature sensors in the gas phase, as well as temperature sensors in the liquid phase, a sensor that measures the water depth and, finally, 100 dynamic pressure sensors that measure the wave impact pressures. For more information on the ATM facility, we refer the reader to Novaković *et al.* (2020) and Ezeta *et al.* (2023).

In figure 1(d) we show a sketch of the flume along with the relevant control parameters and measurement systems. We create a breaking wave in two steps. Firstly, a repeatable solitary wave is produced from a single stroke of the wavemaker using the procedure outlined in Guizien & Barthélemy (2002), where the asymptotic solutions of Grimshaw (1971) are used to calculate the wavenumber, free surface elevation at rest and the propagation speed. For a comprehensive review of the wave generation, we refer the reader to Ezeta *et al.* (2023). The shape of the wave is quasi-two-dimensional, since the wavemaker spans the entire channel width and the side effects at the channel walls may be neglected, noting that in the propagation time of the wave (<10 s) the viscous boundary layer at the channel walls may have grown to a width of <3 mm in the impact area, which is negligible compared with the width of the flume (60 cm). Secondly, to subsequently induce the breaking of the solitary wave, a bathymetry profile has been installed in front of the impact wall, which we called the ‘beach’. This ‘beach’ is made of stainless steel and

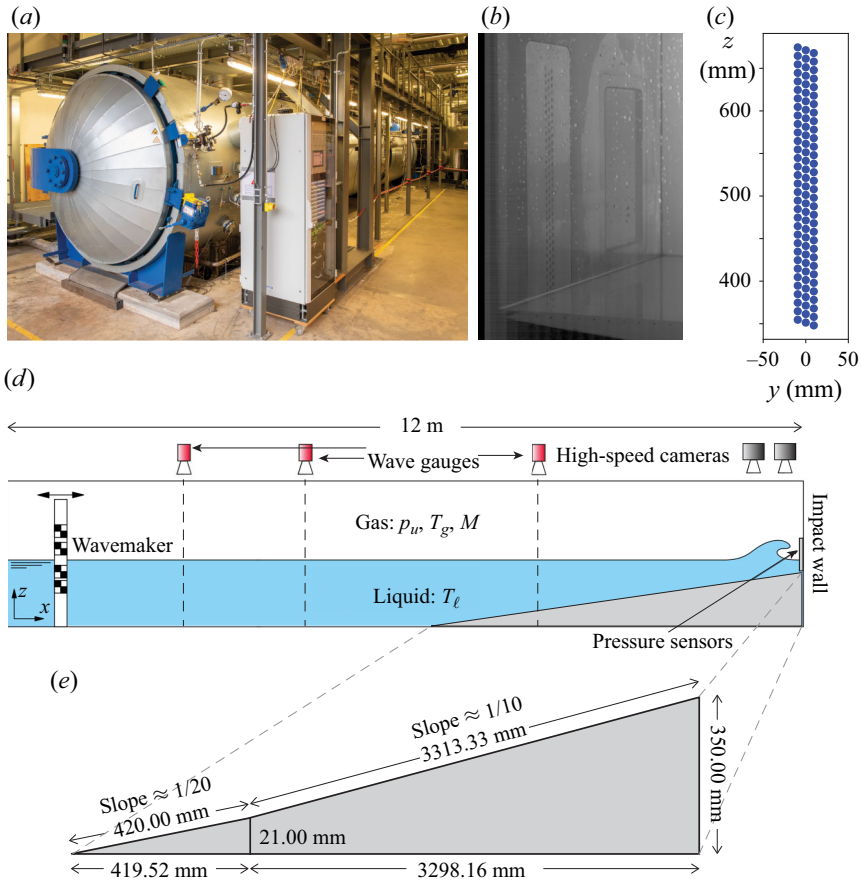


Figure 1. (a) The autoclave of the ATM facility at MARIN. (b) Impact wall with sensor array on the metal plate in the left of the picture (note that the right structure is a window). (c) Arrangement of the pressure sensors on the impact wall, when looking from the flume. (d) Sketch of the flume inside the autoclave along with the control parameters for both the liquid and gas. (e) Sketch of the metal beach located in front of the impact wall, with main dimensions.

its dimensions can be seen in figure 1(e). This procedure results in reproducible breaking waves, as discussed in great detail in Ezeta *et al.* (2023).

The impact wall is equipped with 100 Kistler piezoelectric pressure sensors (type 601CAA) that measure the impact pressures at an acquisition rate of 200 kHz. Each sensor has a circular pressure sensitive area with a diameter of $D_s = 5.5$ mm. The amplification, digitization and scaling of the signals in units of bar are done by 25 Kistler amplifiers (LabAmps, type 5165A) (i.e. four pressure sensors per LabAmp) that are connected to the acquisition system of the ATM. The 100 pressure sensors are mounted onto a vertical metallic plate on the impact wall. The sensitive membranes of the sensors are all flush with the impact wall and their locations can be found in figure 1(b,c). The pressure sensors are arranged in three linear arrays that are slightly shifted with respect to one another such that they form a densely packed array. When looking from the flume, and when sensors are ordered along their increasing vertical position, each subsequent sensor has a vertical distance of $\Delta z = 3.3$ mm to the previous one, and a horizontal distance of $\Delta y = 9.4$ mm to the left. For the sensors in the rightmost vertical linear array, however, the horizontal

distance is $\Delta y = 18.9$ mm to the right (see [figure 1c](#)). Most importantly, the vertical positions of the sensors are distributed evenly over the measurement range.

3. Experimental results

Before turning to the discussion of the main experimental results, we first take some time to introduce the measurement procedure and the parameter settings used in this work in some greater detail. After that we compare a single experiment in the water–vapour thermal equilibrium conditions (i.e. in a boiling liquid) with a corresponding one in water and air. This section ends with a comparison of the wave impacts at different parameter settings for our boiling liquid system.

3.1. Experimental protocol and parameter settings

The main goal of this series of experiments is to investigate the role of condensable gases (vapour) during the impact of a boiling liquid (water), i.e. a liquid that is in thermal equilibrium with an environment that consists of its own vapour. This necessarily implies that once the equilibrium temperature is chosen, the equilibrium pressure follows directly from the vapour curve of the liquid. We have used six different temperatures, namely $T_0 = 20, 30, 40, 50, 60$ and 70 °C. After setting the temperature in the autoclave, we allow the system (typically for a period of 12 h) to equilibrate to the corresponding vapour pressures $p_0 = p_{V,0} = 23.3, 42.3, 73.6, 123.0, 198.6$ and 310.8 mbar, respectively. Subsequently, we perform approximately 10 experimental runs for three different wave shapes, characterised by the parameter α introduced in Ezeta *et al.* (2023), which corresponds to the wave steepness of the solitary wave before it reaches the beach, defined as $\alpha = A/h_l$, where A is the amplitude of the solitary wave and h_l the (quiescent) liquid height inside the flume. For the purpose of this work, the liquid height was fixed to $h_l = 365$ mm, and measured as $h_l = 365.0 \pm 0.3$ mm over the entire experimental series of approximately 180 experimental runs, where the error has been taken equal to the standard deviation of the sample. The chosen values for the wave steepness are $\alpha = 0.350, 0.385$ and 0.420 , which correspond to a cross-sectional area of the entrapped vapour or gas pocket of $A_{cross} = 2.7 \pm 0.7, 9.5 \pm 0.9$ and 17.4 ± 1.0 cm², respectively. Note that the relatively large error is mainly due to inaccuracies in tracing the pocket shape from the high-speed recordings.

The impact of the wave onto the impact wall is recorded with two high-speed cameras, located outside of the autoclave and imaging through two windows with backlighting from the other side, recording at 4000 frames per second at a resolution of 1024 by 1024 pixels². The side walls of the flume are made out of glass such that the wave can be imaged from the outside. One of the cameras captures a side view of the impacting wave, which allows us to reconstruct the shape of the wave, and the size of the captured vapour pocket as a function of time, making use of the quasi-two-dimensional shape of the wave. The other camera takes an oblique view of the impact, which serves to verify the quasi-two-dimensional character of the impact and in addition allows us to appreciate the dynamics of the entrapped vapour pocket in greater clarity.

The views from the two high-speed cameras allows us to verify that, for each value of α used, the wave shape is repeatable, and that they are reproducible for the different values of T_0 used. This is shown in more detail in [Appendix A](#).

3.2. Comparison of a boiling liquid versus a water-air wave impact

In [figure 2](#) we show two snapshots from a water-wave impact with wave steepness $\alpha = 0.385$ in air under atmospheric conditions at $T_0 \approx 20$ °C and $p_0 \approx 1.0$ bar in

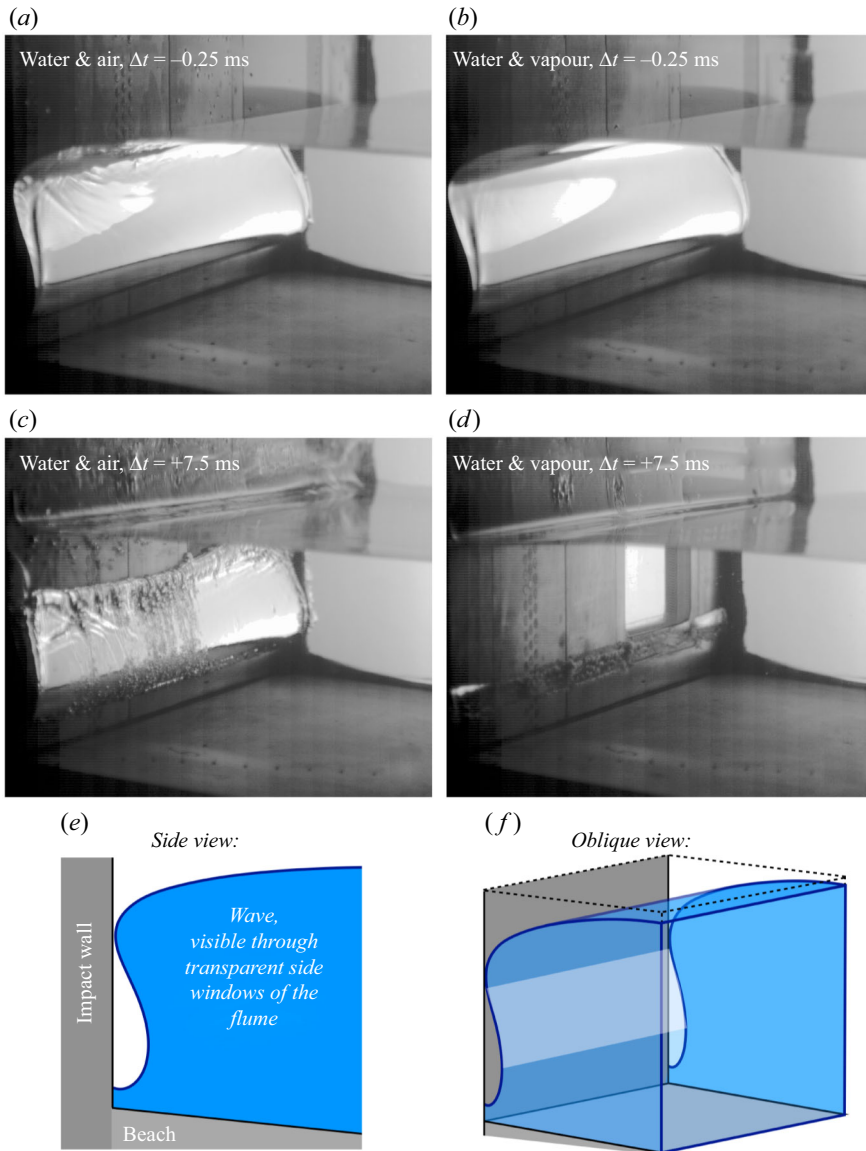


Figure 2. Two snapshots from an experiment in water and air (*a,c*) at $T_0 \approx 20^\circ\text{C}$ and atmospheric pressure $p_{atm} = 1$ bar, taken just before impact and 7.8 ms later, compared with snapshots from a similar experiment with the same wave shape in a boiling liquid (i.e. water and water vapour at equilibrium); (*b,d*) at $T_0 \approx 20^\circ\text{C}$ and $p_0 \approx p_V(T_0) = 23.3$ mbar. Note that the images are taken from an oblique viewpoint, looking through the wave at the wall of impact, which allows for good observation of the shape of the entrapped cavity, the free surface of which appears as the brightest object in the pictures. In both cases, a solitary wave with wave steepness $\alpha = 0.385$ has been used. Clearly, the wave shapes just before impact (*a,b*) are very similar, whereas 7.8 ms later there is an entrapped air pocket visible in the air case (*c*), whereas the vapour pocket in the boiling liquid case has nearly completely vanished. (*d*). A sketch of the side view of the wave just before impact is provided in (*e*), and the oblique view – looking from the flume towards the impact wall – that is also taken in (*a-d*) is sketched in (*f*). Note that the wave can be observed through small windows in the autoclave since the side panels of the flume are made of glass. For a better visual comparison, see supplementary movie 1 comparing the impact in air and vapour available at <https://doi.org/10.1017/jfm.2025.110>.

comparison with two snapshots at comparable times for a water-wave impact of the same wave shape in boiling liquid conditions at $T_0 \approx 20^\circ\text{C}$ and $p_0 \approx p_V(T_0) = 23.3$ mbar. Note that the measured values of liquid and air temperature and air pressure were $T_l = 18.4^\circ\text{C}$, $T_g = 20.9^\circ\text{C}$ and $p_0 = 1.015$ bar, respectively, in the atmospheric case and $T_l = 20.1^\circ\text{C}$, $T_g = 19.9^\circ\text{C}$ and $p_0 = 26.1$ mbar, respectively, for the boiling liquid case. For $T_0 \approx 20^\circ\text{C}$, $p_0 = 25.9$ mbar was the closest we could get to the nominal vapour pressure $p_{V,0} = 23.3$ mbar, which is probably due to a combination of thermal inhomogeneities in the system and some residual non-condensable gas present in the system. Note that, although the smallest pressure that can be reached by our vacuum pump is about 4 mbar (in a system devoid of water), the pump is pumping continuously for several hours, with water continuously supplied to the flume to keep the liquid height h_l constant, such that the remaining partial pressure of non-condensable gases is likely much smaller than 4 mbar. Throughout this work, we use p_0 for measured values of the ambient pressure and $p_{V,0}$ whenever referring to the expected vapour pressure, computed from the temperature T_0 , i.e. $p_{V,0} = p_V(T_0)$. See [Appendix C](#) and [figure 19](#) for an overview of these set points. Wherever we denote a pressure in capitals, it stands for the gauge pressure as it is measured by the pressure sensors, i.e. $P = p - p_0$, where p_0 is the ambient pressure inside the autoclave.

In [figures 2\(a\)](#) and [2\(b\)](#) we observe the two waves just before impact (at $\Delta t = t - t_{\text{impact}} \approx -0.25$ ms, with t_{impact} the time of impact and t time), where we take the oblique view from the flume towards the impact wall that is also sketched in [figure 2\(e,f\)](#). It is clear that there are no obvious visual differences between the two snapshots, owing to the very good reproducibility of the wave shape, even with the greatly varying ambient pressures in the two systems (1 bar vs 26 mbar). So, just before impact the wave shapes are very similar and, as a result, the size of the gas/vapour pocket that is about to be entrapped in the two cases is very similar as well. At $\Delta t = 7.5$, i.e. 7.8 ms later, things look very different in the two cases. Whereas in the water–air case ([figure 2c](#)) an air pocket has been entrapped, which at that time has reached its typical size; for the boiling liquid, one observes in [figure 2\(d\)](#) that the entrapped vapour pocket has almost completely vanished. This could partly of course be due to the large difference between the air ($p_0 = 1015$ mbar) and vapour pressure ($p_0 = 26.1$ mbar), which – for similar driving pressures generated by the impact – would allow the vapour pocket to contract much more than the air pocket, namely approximately a factor 4 in radius. However, when looking at the pressure signals, it becomes clear that the picture is more complex than this.

In [figure 3\(a\)](#) we plot the time evolution of the pressure measured in the 32nd sensor, located at a height $z = 455$ mm, in the air case. (The 32nd sensor is the one that is first hit by the wave in the vapour case. In the air case, the first sensor to be hit is in fact the 34th sensor, and the measured pressure (≈ 0.7 bar) is marginally higher than that in sensor 32.) At the moment of impact, the pressure rises steeply (the sharp peak at $t \approx 410$ ms) to a value denoted as P_{max} , which is approximately 0.6 bar, and which is subsequently followed by an oscillating signal with a frequency of approximately $f = 86$ Hz. Even if we measure it at the crest impact location in the liquid, i.e. at some distance from the entrapped pocket, this oscillating signal can be traced back to the oscillation of the air pocket that is entrapped below the impact point. Using Minnaert's relation for the eigenfrequency of a cylindrical bubble of radius R , namely $Rf = 1.10 \text{ m s}^{-1}$ (Ilinskii *et al.* 2012), this frequency corresponds to a cylindrical bubble radius of $R = 1.28$ cm. This is about a factor two smaller than the actual effective radius of the entrapped cavity, defined as the radius of a hemicylindrical cavity with the same cross-sectional area (see also [Appendix B](#)), which was measured to be 2.45 cm. (For comparison, Minnaert's relation $af = 3.26 \text{ m s}^{-1}$ for a spherical bubble with radius a would have given $a = 3.79$ cm.) Note that

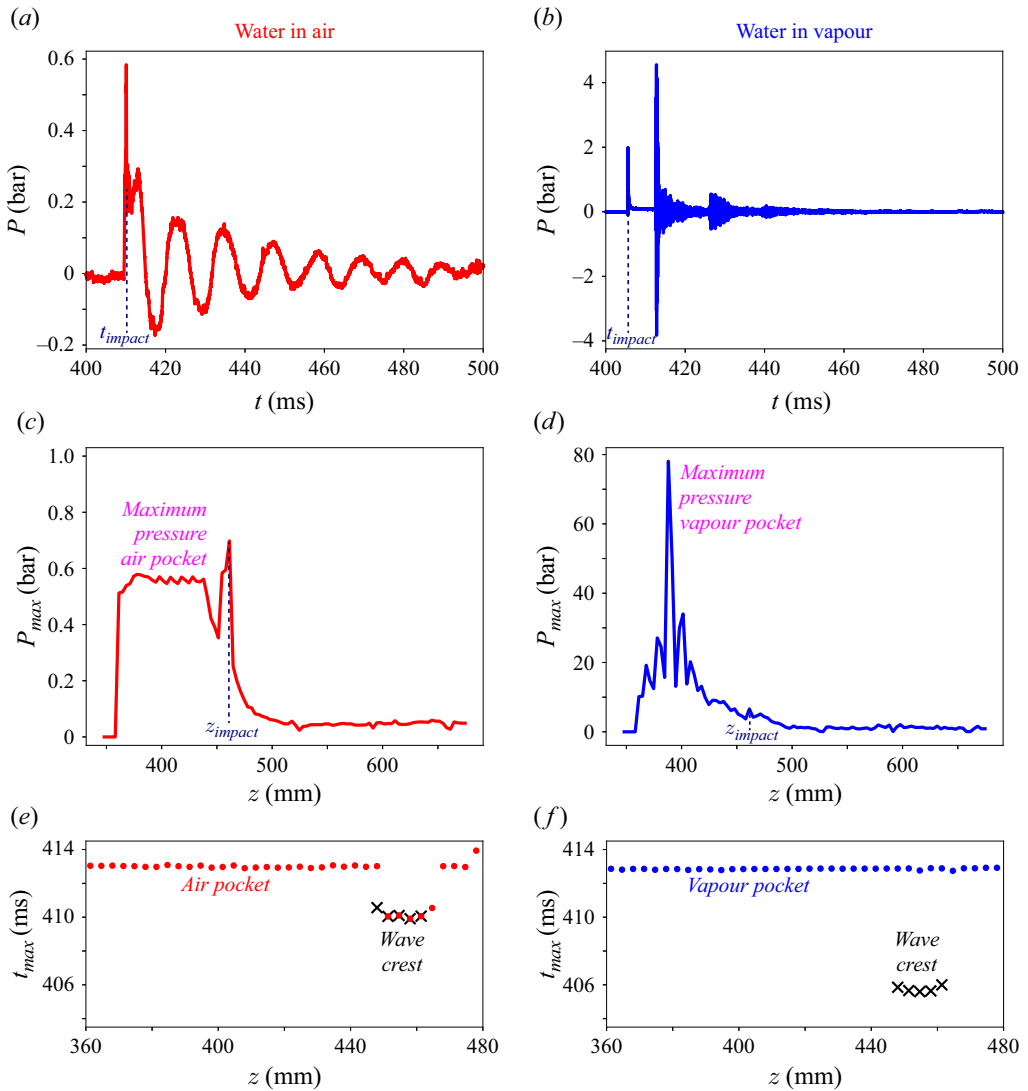


Figure 3. Pressure signals measured for a wave with $\alpha = 0.385$ in the air case (left plots) and the boiling liquid case (right plots). (a,b) Time evolution of the pressure P measured by the 32nd sensor at $z = 455$ mm in the impact wall for (a) the air case and (b) the boiling liquid case. The moment t_{impact} at which the wave crest impacts is indicated by a vertical dashed line in both plots. (c,d) Maximum pressure P_{max} measured in each of the sensors, as a function of its height in the array for (c) the air case and (d) the boiling liquid case. The vertical location z_{impact} at which the wave crest impacts is indicated by a vertical dashed line in both plots. (e,f) Time t_{max} at which the maximum pressure was measured for (e) the air case (red dots) and (d) the boiling liquid case (blue dots). The black crosses indicate the moments in time that the crest impact pressures were measured. Note that pressures are reported as they are measured by the sensors, i.e. as gauge pressures $P = p - p_0$ (denoted with a capital), with p_0 the ambient pressure in the autoclave. This is true for all experimental figures in this work.

the impact pressure is the highest pressure in this time series, which is not surprising, since we are measuring in the point that was first touched by the wave crest, which in air or other non-condensable gases usually gives the largest pressure in a wave impact time series. The surprise is however that when we turn to the equivalent series for the boiling liquid case (figure 3b) we immediately observe that this is no longer true. In fact, the impact is still

visible as the first peak in the time series, at $t \approx 406$ ms, and with $P_{\text{impact}} \approx 2$ bar is even considerably larger than that in the air case, but after that the pressure drops back to a very small value, indicating the absence of pressure building up in the entrapped vapour pocket. That is, until a second, higher peak ($P_{\text{max}} \approx 4.6$ bar) is observed at $t \approx 413$ ms. Since no clear oscillation follows, or possibly extremely rapid ones, this suggests that the vapour pocket has collapsed and that at least a large part of it must have condensed in the process, leaving small gas or vapour fragments that regrow and subsequently collapse in a second, smaller event, or even series of events, starting at $t \approx 426$ ms. See supplementary movie 1 comparing the impact in air and vapour corresponding to figure 2.

The sequence of events suggested above is confirmed in figure 3(d), where the maximum pressure P_{max} observed in the time series of each of the pressure sensor channels is plotted as a function of the sensor height z . Here it becomes clear that the maximum pressure measured at the impact height is completely dwarfed by the maximum pressure measured in the system, which occurs at $z = 388$ mm and equals $P_{\text{max}}(z_{\text{max}}) = 78.1$ bar. This location nicely corresponds to the location of the collapse of the vapour pocket in the high-speed imaging recordings, available in the supplementary movies. Comparing this value to those obtained in the air case (figure 3c), it is clear that pressures obtained in the boiling liquid case are up to two orders of magnitude larger than in the air case. In fact, in the latter the pressure that can be attributed to the wave crest impact is globally the largest in the system, and the pressure oscillations in and around the air pocket are smaller, even if they are quite uniformly spread over a larger area (corresponding to the size of the vapour pocket) and a larger time span. This is in sharp contrast to the boiling liquid case where the crest impact pressure corresponds not even to the maximum in its own time series (figure 3b), and therefore, not even discernable in figure 3(d).

It is instructive to look at the times t_{max} at which the pressure maxima are reached in the different sensors, which are plotted in figures 3(e) and 3(f), where we restricted ourselves to heights < 480 mm, since sensors above that height are in the gas or vapour phase where insignificant signals are obtained. For the air case, we observe that, for small heights (i.e. within the air pocket), the maximum pressure occurs at $t = 413$ ms, whereas around the crest impact point, the first maximum already occurs at $t = 409.9$ ms (red dots in figure 3e). For the boiling liquid case, all pressure maxima occur at $t = 412.8$ ms (blue dots in figure 3f), but due to the separation of the crest impact event and the vapour pocket collapse in time, it is feasible to determine the impact pressure maxima by restricting the search to the time interval before the collapse. This yields the black crosses that indicate the time t_{impact} when the crest impact pressures were recorded. In the air case, t_{impact} coincides with t_{max} , but for the boiling liquid case, $t_{\text{impact}} = 405.6$ ms, which is earlier than t_{max} . Note that in air, the time span between impact and maximum air pocket compression (which can be equated with the maximum pressures measured in the area below the impact) is $t_{\text{impact}} - t_{\text{max}} \approx 3.1$ ms, which is considerably smaller than the corresponding time span in the boiling liquid case ($t_{\text{impact}} - t_{\text{max}} \approx 7.2$ ms). This is because the time it takes for the air pocket to reach its minimum size is smaller than the time the vapour pocket needs to collapse to an almost vanishing length scale.

At this point it is good to stress that the origin of absolute time has no special significance since it depends on a rather arbitrary triggering of the cameras determined by the wavemaker stroke. The fact that the absolute bubble collapse/compression times are close in this case is therefore purely coincidental and has no physical significance.

To finalise our discussion of the impact of a single wave in the water–air and boiling liquid cases we turn to the so-called pressure map, a space–time plot of the signal in the

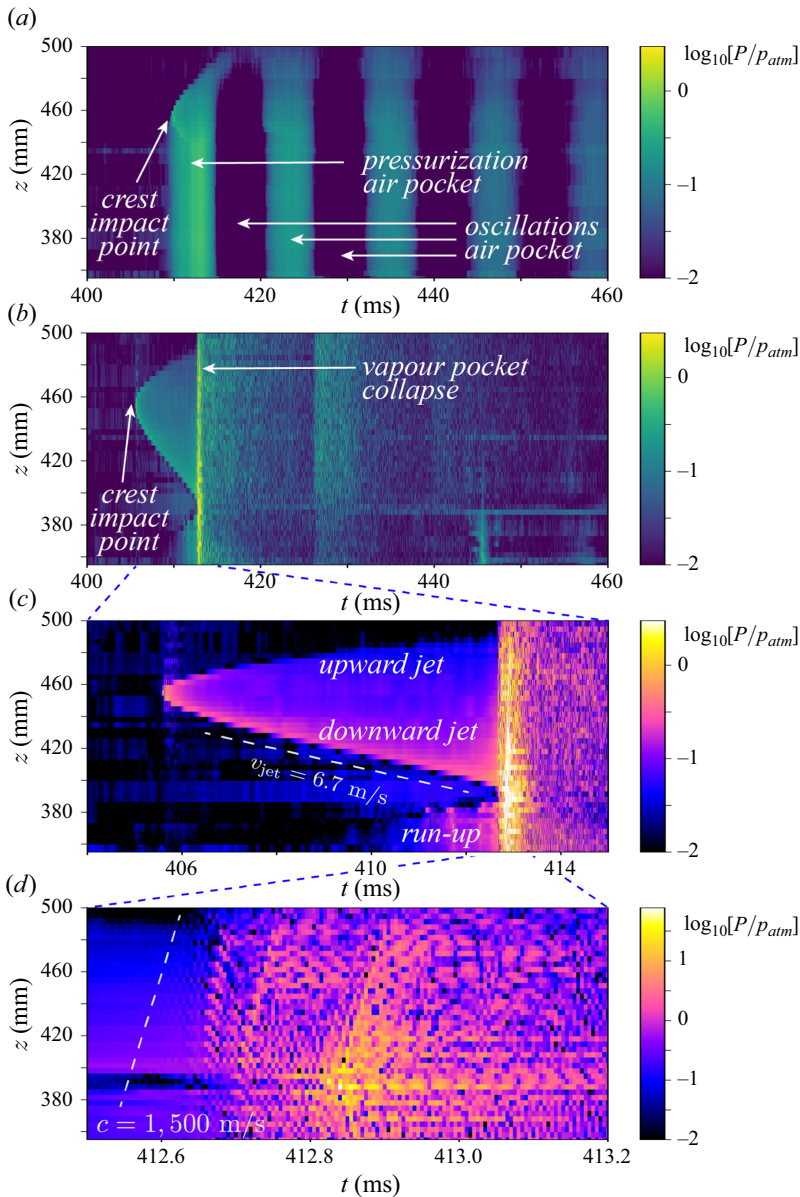


Figure 4. (a) Pressure map $P(z, t)$ of the impact of the same breaking wave in water–air conditions at $T_0 = 20\text{ }^\circ\text{C}$, with $\alpha = 0.385$ also reported in figures 2(a,c) and 3(a,c,e), focusing on the time span from $t = 400 - 460$ ms, containing crest impact, pressurisation of the air pocket and oscillations. Note that pressure is denoted by a logarithmic colour scale, where $p_{atm} = 1$ bar. Also note that all pressures smaller than 0.01 bar are denoted by the same colour as $P = 0.01$ bar, to avoid the noise level. (b) Pressure map $P(z, t)$ of the impact of the same breaking wave, but now in boiling liquid conditions (as reported in figures 2(b,d) and 3(b,d,f)), in the same time interval, containing crest impact and vapour pocket collapse. (c) Same data as in (b), but now horizontally zoomed in on impact (ELP1), jet propagation along the walls (ELP2) and the main vapour pocket collapse event (ELP3). The white dashed line, with approximately the same slope as the propagating downward jet, corresponds to a velocity $v_{jet} = 6.7\text{ m s}^{-1}$. (d) Same data as in (c), but now zoomed in on the vapour pocket collapse event. The slope of the white dashed line in this plot corresponds to the sound speed in water, $c = 1.5 \times 10^3\text{ m s}^{-1}$. Note that the vertical axis is the same in all four plots and zooming was done exclusively along the time axis.

pressure sensor array in our impact wall, provided in [figure 4](#). The upper plot shows the air water case: first, the direct impact of the wave crest as the leftmost point in which high pressures are observed in [figure 4\(a\)](#). This is the point that in wave impact literature has become known as ELP1, where the abbreviation ‘ELP’ is short for elementary loading process (Lafeber *et al.* 2012; Dias & Ghidaglia 2018), and is associated with the combination of the incompressible, and even compressible, impact of the liquid mass onto the wall (Wagner 1932; Lesser 1981; Korobkin 2004). Generally, due to its short duration in time and localisation in space, ELP1 is sometimes hard to resolve, but in this case we verified that, owing to the time resolution of our sensors (5 μ s), we indeed have. From that point onwards, liquid jets start spreading upwards and downwards along the impact wall, a pressure signal known as ELP2, of which the upward one is clearly visible in the upper figure. The downward one is a bit obscured by the pressure build up in the air pocket, which in recent wave impact literature (Lafeber *et al.* 2012; Dias & Ghidaglia 2018) became known as ELP3, a name that is also associated with the gas pocket oscillations in the air case. These are very visible in the pressure map, although one can only see the positive part of the oscillations due to the fact that for the logarithmic colour scale used, pressures below a threshold of $P = 0.01$ bar are cut off to this value.

The second plot shows the corresponding boiling liquid case ([figure 4b](#)). Again, the leftmost point in which high pressures are observed corresponds to the crest impact, but then the plot is very different from the water–air case. First, there is no pressurisation of the vapour pocket, which remains at a low pressure, which in turn makes the downward jet very visible. A bit more faint, but definitely also discernible is the motion of the lower three-phase-contact line of the entrapped vapour pocket (the so-called run-up), which culminates at the meeting point of the downward jet and run up in a vertical band of very large pressures throughout the entire system at $t = 412.8$ ms connected to the collapse of the vapour pocket. Visible at later times are a second collapse at $t \approx 426$ ms after a first rebound of the vapour pocket (or rather its fragmented remnants after regrowing in the rarefaction period that follows after collapse), and even a third one in the lower part of the system at $t \approx 440$ ms, both of which are also visible in the time series of [figure 3\(b\)](#). Most importantly, the oscillations that dominate the water–air case are absent.

When we zoom in onto the region between impact and vapour pocket collapse ([figure 4c](#)), we clearly observe the high speed with which the liquid jet moves downwards along the impact wall, with a velocity $v_{jet} \approx 6.7$ m s⁻¹ (white dashed line) that exceeds the impact speed of the wave ($v_{impact} \approx 2.1$ m s⁻¹) by a factor of 3, a factor that depends on the radius of curvature of the wave crest. The estimation of v_{impact} is shown in [Appendix B](#). Very different from what is observed in the air case, where the entrapped air pocket is pressurised as soon as the wave impacts the wall, the pressure inside the vapour pocket remains negligible during collapse, which is a strong indication that the vapour present in the pocket is in fact condensating instead of compressing. Following the signal in a single pressure sensor, e.g. at height $z = 420$ mm, the pressure remains small and close to the background noise level of the sensor until $t \approx 409.5$ ms. After this time, the sensor becomes wetted and the pressure suddenly rises to a level of about 0.2 bar, where it remains until the vapour pocket collapses and the pressure rises to 10 bar.

Finally, we zoom in even more in [figure 4\(d\)](#), where we focus on a time span of about 700 μ s around the collapse of the vapour pocket. The first thing to notice in this plot are the diagonal lines that radiate out from the collapse point, which is approximately located at $z = 388$ mm in space and at $t = 412.85$ ms in time. These diagonal lines have a slope that is consistent with the speed of sound in water $c = 1500$ m s⁻¹ indicated by the white dashed line in this plot. Therefore, we may conclude that these diagonal lines correspond to pressure waves emanating from the collapse point. Having said this, one may wonder

why there are diagonal lines in the same plot that seem to originate at a point in time before the collapse of the cavity. To understand their origin it is good to realise that the system has a third dimension and that due to slight but unavoidable asymmetries along the horizontal axis parallel to the wall (the y axis of our system), the collapse does not necessarily happen at the same point in time along that axis. So some nearby part of the cavity may already have collapsed, where the pressure is generated by the inertial collapse of the liquid onto part of that axis, which may induce large pressure signals already slightly before the collapse takes place in the region of the pressure sensor array. In fact, the one structure close to the dashed line with a larger slope than c may be due to an event having taken place at some distance, such that the signal arrives at the pressure sensors more simultaneously as it would when the event had taken place on the sensor array.

In addition, we highlight other remarkable features in this plot. Firstly, when looking at subsequent sensor heights, i.e. subsequent horizontal lines in the diagram, one often observes a pattern that seems to repeat itself every third sensor and in both directions (upwards and downwards). This is likely connected to the threefold structure of the sensor arrangement (cf. [Figure 1c](#)), where every third sensor is located exactly above (or below) the sensor from which one started, whereas distances in the y direction are slightly larger. Secondly, there are clear oscillations in the signal, for which we may estimate the frequency to be of the order of 40 kHz, i.e. considerably smaller than the acquisition rate of the pressure sensors (200 kHz). This may be due to structural oscillations in the impact plate in which the sensors are embedded or small gas/vapour bubbles.

To conclude this subsection, we find that pressures measured in boiling liquid breaking wave impact may be up to two orders of magnitude larger than those in air. This enormous difference can be traced back to the collapse of the entrapped vapour pocket. Condensation of vapour is likely to strongly contribute to this phenomenon, since condensation depletes the vapour pocket of content, which facilitates its violent collapse.

3.3. Comparison of pressure characteristics for different temperatures and wave shapes

We now turn to the description of the dependence of the vapour pocket and impact pressures on temperature and wave shape in [figure 5](#), where we plot the maximum value $P_{max}(z)$ of the measured pressure time series for each of the pressure sensors, as a function of the vertical sensor position z , and for each of the approximately 10 experiments performed for every parameter setting (blue-shaded dots). Note that the data from [figure 3\(d\)](#) is also one of the 10 experiments plotted in [figure 5\(a\)](#), and that we removed the data above $z = 550$ mm since those are in the vapour phase for each wave shape and not measuring anything worth showing. In each of the panels in [figure 5](#) we also present the average of the approximately 10 experiments, indicated by the black lines.

In addition, in the analysis below we make use of the fact that pressures caused by the crest impact and those caused by entrapped vapour pocket dynamics are temporally and spatially separated (cf. [Figure 3e,f](#)), such that we can define the maximum vapour pocket pressure (P_{pocket}) as the maximum pressure associated with the vapour pocket dynamics (due to collapse or compression), averaged over all 10 experiments performed at a single parameter setting and the maximum crest impact pressure (P_{crest}), obtained by first averaging the three largest pressures measured during the impact stage for each experiment and subsequently averaging over the 10 individual experiments for each parameter setting.

We start with the discussion of the temperature dependence of the maximum vapour pocket pressure and maximum crest impact pressure for a breaking wave with wave steepness $\alpha = 0.385$, under boiling liquid conditions. In [figure 5](#) we show the results for the maximum pressure $P_{max}(z)$ measured in each of the pressure sensors on the impact wall,

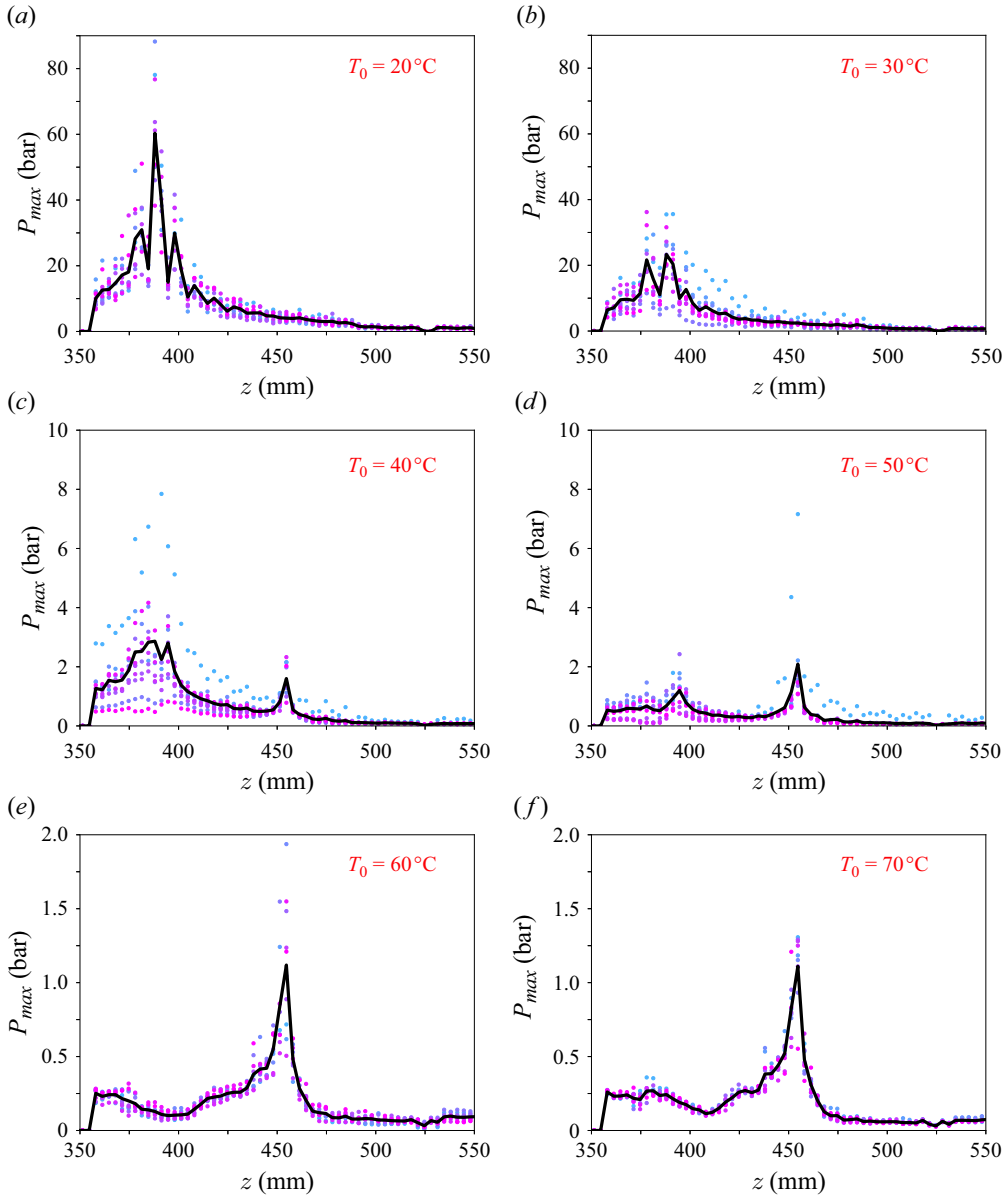


Figure 5. Maximum pressure $P_{max}(z)$ measured as the maximum in the time series of each sensor and plotted as a function of the vertical sensor location z at the impact wall under boiling liquid conditions, for a breaking wave with wave steepness $\alpha = 0.385$ and for six different ambient temperatures ranging from $T_0 = 20^\circ\text{C}$ to 70°C , corresponding to (a) to (f), respectively. For each experimental setting, there were approximately 10 repetitions of the experiment. In each panel, the blue-shaded dots correspond to the individual experiments, whereas the solid black line corresponds to their average. Note that the pressure range (vertical axis) is largest in (a,b) and decreases for (c,d) and (e,f). Movies comparing the wave impact in boiling liquid conditions for these six temperatures are available for $\alpha = 0.385$ (corresponding to this figure) and $\alpha = 0.420$ in the supplementary movies.

as a function of their height z , for temperatures increasing from $T_0 = 20^\circ\text{C}$ to 70°C . At $T_0 = 20^\circ\text{C}$, with vapour pressure $p_{V,0} = 23.3$ mbar, the pressures are clearly the largest, with an average maximum value of $\langle P_{pocket} \rangle = 60$ bar (maximum of the black curve)

and individual measurements reaching up to 88 bar (blue-shaded dots). While the largest pressure occurs at the height where the pocket collapses, namely $z_{coll} \approx 388$ mm, nothing can be discerned at the location where the wave impact is expected, at $z_{impact} \approx 455$ mm. This is consistent with the fact that even there the recorded maximum pressures, with $P_{max}(z_{impact}) \approx 4\text{--}5$ bar, are much larger than the crest impact pressures ($P_{impact} < 2$ bar).

Increasing the ambient temperature in liquid and vapour to $T_0 = 30$ °C, corresponding to a vapour pressure $p_{V,0} = 42.3$ mbar, the average maximum vapour pocket pressure clearly decreases to $\langle P_{pocket} \rangle = 27$ bar, but otherwise the data are similar as in the $T_0 = 20$ °C case, with pocket collapse being the dominant feature in the plot and no visible signal from the direct impact of the wave crest. Remarkable in both plots are the multiple peaks that are visible in the collapse region. Since these are both present in the average and in the individual data series (e.g. as in figure 3d), this cannot be due to variability of the height at which the vapour pocket collapses: the collapse seems to occur at the same location ($z_{coll} \approx 388$ mm) for all repetitions of the same conditions. In fact, the multiple peaks reveal again the apparent ‘threefoldness’ due to the sensor arrangement that we previously pointed out. This further supports the idea that the collapse pressures are not uniform in the spanwise (y) direction along the impact wall.

At $T_0 = 40$ °C, corresponding to a vapour pressure $p_{V,0} = 73.6$ mbar, in figure 5(c) we see drastic changes: overall pressures are much smaller (note the change in the pressure scale from 0–90 bar down to 0–10 bar). In contrast to lower temperatures, the crest impact pressure is now discernible as a very clear peak at $z_{impact} \approx 455$ mm, where the maximum pressures reach up to about $P_{impact} \approx 2$ bar. Furthermore, looking at the collapse region, one sees a diversified picture: whereas in some experimental realisations hardly any collapse pressure is measured (lower blue-shaded data points), in other ones maximum collapse pressures reach up to 8 bar thus revealing a large variability near the collapse region. The average maximum vapour pocket pressure decreases to $\langle P_{pocket} \rangle = 3.8$ bar.

This trend continues in the data of $T_0 = 50$ °C, corresponding to a vapour pressure $p_{V,0} = 123.0$ mbar, where the impact pressure is now even better discernible. Although the vapour pocket collapse is still a clear feature in most experimental realisations, with an average maximum pressure in the collapse region of $\langle P_{pocket} \rangle = 1.3$ bar, it is now for the first time smaller than the average maximum crest impact pressure, which equals $\langle P_{crest} \rangle = 1.5$ bar. Interestingly, this suggests the existence of a transition temperature in which both the collapse and impact pressure are nearly the same. For this wave shape, this temperature lies within $T \in [40, 50]$ °C. Note in addition that there is a very large crest impact pressure of approximately 7 bar, which (without clear evidence) we tentatively attribute to the presence of a small entrapped vapour pocket during impact that upon implosion is responsible for the extreme impact pressure. It is good to note that such a large crest impact pressure has only been recorded in 1 out of the total of 181 impact experiments we conducted in boiling liquid conditions during this campaign.

Finally, figure 5(e,f), at $T_0 = 60$ °C (with $p_{V,0} = 198.6$ mbar) and $T_0 = 70$ °C ($p_{V,0} = 310.8$ mbar), provides a similar picture: in these plots, where the vertical axis now only ranges from 0 to 2 bar, it is observed in both cases that the impact pressure is dominant, with average maximum crest impact pressures of $\langle P_{crest} \rangle = 1.2$ bar. In the region where for lower temperatures a vapour pocket collapse was observed ($z \approx 360\text{--}410$ mm), pressures are of the order of a few tenths of a bar, without the prominent peak that was observed for $T \leq 30$ °C.

It is good to stress that pressures measured in the boiling liquid case are so large that, when comparing the similar plot for the water–air impact (figure 3c) to the data in figure 5,

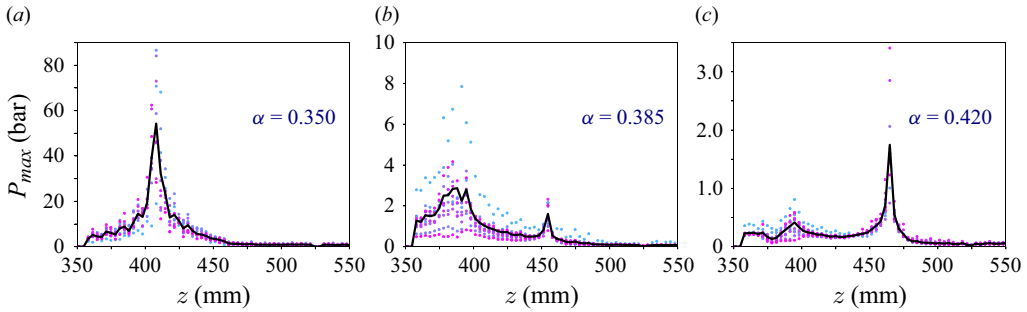


Figure 6. Maximum pressure $P_{max}(z)$ measured in each sensor as a function of the sensor location z at the impact wall under boiling liquid conditions at an intermediate ambient temperature $T_0 = 40\text{ }^\circ\text{C}$ ($p_{V,0} = 73.6\text{ mbar}$), for three breaking waves with wave steepness $\alpha = 0.35, 0.385$ and 0.42 , corresponding to (a), (b) and (c), respectively. For each experimental setting, there were 10 repetitions of the experiment. In each panel, the blue-shaded dots correspond to the individual experiments, whereas the solid black line corresponds to their average. Note that the pressure range is largest in (a) and decreases towards (c).

the data would almost coincide with the horizontal axis in figure 5(a,b), would reach up to 7% of the height of the figure 5(c,d) and would only be clearly visible in the figure 5(e,f).

Now, a first conclusion one can draw is that, as temperature and vapour pressure increase, the entrapped vapour pocket collapses in a less violent manner, leading to strongly decreasing collapse pressures as the temperature increases. This is however not yet the complete story. As soon as one considers the wave shape in the analysis, it becomes clear that the latter also plays a significant role.

In order to evaluate the wave shape dependence, we show in figure 6 the measurement of $P_{max}(z)$ at a fixed temperature ($T_0 = 40\text{ }^\circ\text{C}$) and for all three wave shapes ($\alpha = 0.350, 0.385, 0.420$). Here, we observe an extremely strong vapour pocket collapse for the $\alpha = 0.350$ case, with an average maximum vapour pocket pressure of $\langle P_{pocket} \rangle = 56\text{ bar}$, of the same order as that observed at the lowest temperature for $\alpha = 0.385$. For the intermediate case ($\alpha = 0.385$), we find a very clear presence of both vapour pocket collapse and wave crest impact pressures, as already discussed above. In contrast, for $\alpha = 0.42$ in figure 6(c), the impact pressure is dominant, with an only very moderate but nevertheless clearly distinguishable average maximum vapour pocket pressure of $\langle P_{pocket} \rangle = 0.45\text{ bar}$. It is also worth noting that the crest impact and vapour pocket collapse locations are clearly changing, namely from $z_{impact} = 439\text{ mm}$ through 455 mm to 464 mm , and from $z_{coll} = 407\text{ mm}$ through 388 mm to 390 mm , respectively, from $\alpha = 0.35$ through 0.385 to 0.42 .

In figure 7 we compare the average maximum vapour pocket pressure $\langle P_{pocket} \rangle$ for all three investigated wave shapes as a function of ambient temperature, where the pressure axis is logarithmic. For the wave shape that entraps the smallest vapour pocket ($\alpha = 0.35$), collapse pressures remain very high ($\geq 50\text{ bar}$) up to $T_0 = 50\text{ }^\circ\text{C}$, and only start to drop for the highest two ambient temperatures in our sample, where vapour pocket collapse pressures reach values below 10 bar . From the very large error bars for these last two points one can conclude that there is quite a bit of variation between single realisations, and indeed for some experiments we observe collapse pressures close to 10 bar , whereas in others a vapour pocket collapse appears to be completely absent (not shown).

For the intermediate vapour pocket case ($\alpha = 0.385$) at the lowest ambient temperature ($T_0 = 20\text{ }^\circ\text{C}$), the average maximum vapour pocket pressure $\langle P_{pocket} \rangle$ is of the same order of magnitude as that for $\alpha = 0.35$, but then almost exponentially decays with temperature, until a minimum value of $\approx 0.25\text{ bar}$ is reached, where it subsequently remains. For

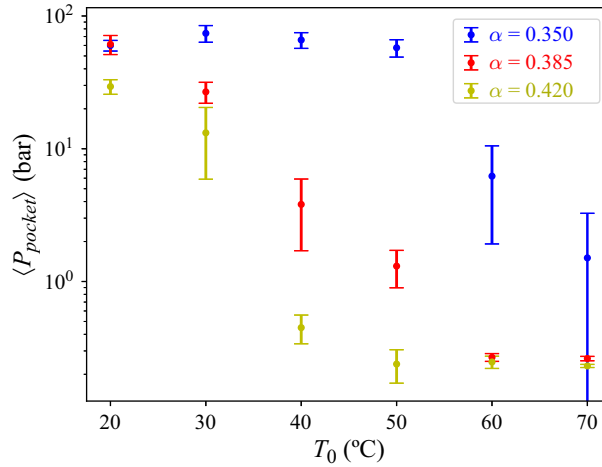


Figure 7. Maximum vapour pocket pressure $\langle P_{pocket} \rangle$, averaged over all 10 experiments performed at a single parameter setting, plotted as a function of ambient temperature T_0 for all three investigated wave shapes $\alpha = 0.35$ (blue), 0.385 (red) and 0.42 (yellow). The symbols represent the average over the individual experiments (data not shown), and the error bars are twice the standard deviation of the sample and would be symmetric on a linear scale.

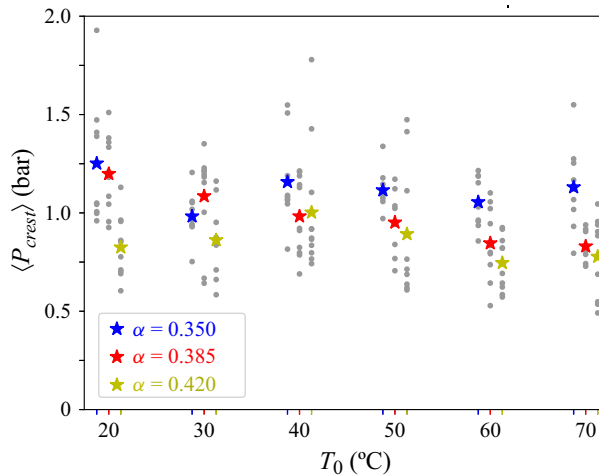


Figure 8. Average maximum crest impact pressure $\langle P_{crest} \rangle$ as a function of ambient temperature T_0 for all three investigated wave shapes $\alpha = 0.35$ (blue), 0.385 (red) and 0.42 (yellow). The quantity $\langle P_{crest} \rangle$ has been obtained by first averaging the three largest pressures measured during the impact stage for each experiment (represented by grey dots) and subsequently averaging over the 10 individual experiments for each parameter setting, denoted by the coloured stars. Note that we have horizontally shifted the data for the three wave shapes for clarity of presentation.

the largest pocket ($\alpha = 0.42$), the largest pressures are not even reached for $T_0 = 20$ °C. Here, the decay with temperature is similar to the other two wave steepnesses, but the minimal value is reached earlier and sustained up to the largest ambient temperature in our measurements.

For completeness, in figure 8 we also present the average maximum crest impact pressures $\langle P_{crest} \rangle$, measured during the crest impact stage. To define those, for each

experiment, we first identify the three pressure channels containing the largest pressures measured during the crest impact stage, and subsequently average those three maximum pressures. These are represented by the grey dots. The coloured, star-shaped symbols in turn constitute the averages of those values for each experimental setting (α , T_0). Note that we discarded the one instant of a very large impact pressure measured at $\alpha = 0.385$ for $T_0 = 50$ °C discussed above in the average. As becomes clear from the data, $\langle P_{crest} \rangle$ shows much less variation with temperature as the maximum vapour pocket pressure, indicating that it is less affected by phase change. For all experiments, the averages lie between 0.8 and 1.3 bar. There may be a slight decreasing trend with temperature, but it is only convincing for the average data for $\alpha = 0.385$, and it is clear that the spread in the individual data points is too large to reliably corroborate the trend.

To conclude the section, we want to stress that in this work we have focused on the experimental characterisation of the pressure, instead of other parameters such as the force or the impulse during impact, which are also relevant parameters in many applications involving impacts. Nevertheless, we did numerically integrate the measured pressures over the height of the wall and multiplied with the width of the flume to obtain the force time series $F(t)$, for which we could determine the maximum F_{max} , the timing of which coincides with the vapour pocket collapse in the case such a collapse occurs. For $T_0 = 20$ °C, this leads to $F_{max} \approx 20\text{--}50$ kN, and by integrating $F(t)$ around the maximum over a time period corresponding to the duration of the peak, we obtain an estimate for the associated impulse $I \approx 3\text{--}5$ Ns. Here, the ratio $I/F_{max} \sim 80\text{--}120$ μs provides an estimate for the duration of the force peak (or an estimate for twice the rise time). This can be contrasted to the values observed for the water–air system, where the maximum in the force signal corresponds to the first pressurisation of the air pocket, leading to an order of magnitude smaller $F_{max} \approx 3\text{--}5$ kN, but slightly larger $I \approx 5\text{--}13$ Ns, owing to the larger duration (rise time) of the air pocket pressurisation ($I/F_{max} \approx 1\text{--}4$ ms). One could say that (at small T_0) the slow momentum transfer occurring during the first air pocket pressurisation in the vapour case is postponed due to condensation and the corresponding momentum change is suddenly imparted onto the wall at the moment the vapour pocket collapses. Note that in all cases the crest impact is too localised in space to contribute significantly to the force.

4. Comparison to a simplified model of the vapour pocket collapse

In the previous section we found that the pressures measured during the collapse of the vapour bubbles in our experiment were varying over two orders of magnitude, both as a function of temperature and as a function of wave shape. In this section we now formulate a simplified model for the vapour bubble dynamics, which we subsequently compare to the experimental observations.

4.1. A simplified model for the vapour pocket dynamics

Inspired by the seminal work of Prosperetti and many others in this field (Prosperetti & Plesset 1978; Prosperetti 2017; Bergamasco & Fuster 2017), we assume that in our case the heat transport into the liquid is the factor that limits phase change for the vapour pockets observed in the experiments. We assume that the vapour bubble is homogeneous for all relevant time scales, which is reasonable given the fact that the heat diffusivity in water vapour is typically at least two orders of magnitude larger than the heat diffusivity in the liquid. In addition, we assume that the bubble is in thermal equilibrium at all times, which stands to reason since the vapour density ρ_V is much smaller than the liquid density ρ_L , such that the heat capacity per unit volume c_p/ρ is much larger for the liquid than for

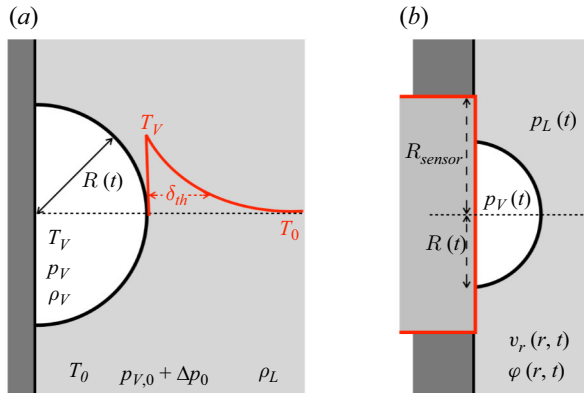


Figure 9. (a) Sketch of the simplified model of the vapour pocket. A hemicylindrical bubble of radius $R(t)$ and length W filled with vapour of density ρ_V , temperature T_V and pressure p_V is in contact with a liquid of constant density ρ_L and temperature T_0 . The pressure in the liquid is the sum of the equilibrium vapour pressure $p_{V,0}$ corresponding to the liquid temperature T_0 and the hydrodynamic pressure $\Delta p_0 = \rho_L V_{wave}^2$ in the liquid. The pressurisation of the vapour bubble triggers condensation, the latent heat of which will be transported into the liquid according to the temperature difference $T_V - T_0$. (b) Sketch of the situation where the bubble is only partially covering the pressure sensor and the pressure p_L in the surrounding liquid needs to be taken into account in addition to the vapour bubble pressure p_V to estimate the measured pressure from the model; see also [Appendix F](#).

the vapour. If the bubble is pressurised, it will then strive to attain back to equilibrium by condensation, where the heat is to be conducted away into the liquid.

Assuming the bubble to be of hemicylindrical shape in an infinite medium with radius R and length W , as sketched in [figure 9\(a\)](#), neglecting the proximity of the free surface of the wave, we may thus write an energy-mass balance equation as

$$L \frac{dm_V}{dt} = S_w k_L \left. \frac{\partial T}{\partial r} \right|_{r=R(t)}, \tag{4.1}$$

where m_V is the vapour mass contained in the bubble, $S_w = \pi R W$ the surface area of the hemicylindrical bubble, L the latent heat of evaporation and k_L the heat conductivity of the liquid. Here, we choose to neglect the volume changes in the liquid due to phase change, since the vapour density was assumed to be much smaller than that of the liquid. Also neglected is the sensible heat of the vapour bubble, in view of the expected smallness of the Jacob number $Ja = c_{p,V} \Delta T / L$, which is of order 8×10^{-3} or smaller for temperature changes below $\Delta T = 10^\circ\text{C}$. Here, $c_{p,V}$ is the heat capacity of the vapour.

In addition, by writing down (4.1), we neglected the heat transport into the impact wall, which is assumed to be adiabatic in the model. This can be shown to correspond to the condition that the wall is dry (i.e. not wetted by the liquid phase) before impact. This assumption is discussed more extensively in [Appendix D](#).

Writing $m_V = V \rho_V = (1/2)\pi R^2 W \rho_V$, where $V = (1/2)\pi R^2 W$ is the volume of the bubble, in (4.1) leads to

$$\left(\frac{\partial \rho_V}{\partial p_V} \right) \frac{dp_V}{dt} = - \frac{2\rho_V}{R} \frac{dR}{dt} + \frac{2k_L}{LR} \left. \frac{\partial T}{\partial r} \right|_{r=R(t)}. \tag{4.2}$$

Physically, there is a competition between the two terms on the right-hand side: suppose, for example, because of a wave impact, that the bubble compresses, the first term states that the pressure will rise when the radius becomes smaller (noting that $dR/dt < 0$). Since the temperature then rises as well, the second term states that condensation heat will be

transported away from the bubble, allowing some of the vapour to condensate and the pressure to decrease. Consequently, if the first term is dominant, the vapour bubble is expected to behave similar to a non-condensable gas bubble, which starts to oscillate after the wave impact, whereas dominance of the second term would lead to effective condensation and, hence, a collapse of the vapour bubble. We will return to this point in more detail in § 4.3.

Since the bubble is assumed to be on the vapour curve at all times, this implies we may choose any thermodynamic state variable to describe the other two, i.e. we may choose $\rho_V = \rho_V(p_V)$ and $T_V = T_V(p_V)$. Using the Clausius–Clapeyron equation and the ideal gas law, the density and temperature of the gas may be expressed in terms of the bubble pressure p_V together with the thermodynamic state variables at equilibrium, $p_{V,0}$, $\rho_{V,0}$ and T_0 , which for convenience is summarised in Appendix C.

The energy-mass balance equation (4.2) is complemented by an equation of motion for the hemicylindrical bubble, for which we take the two-dimensional Rayleigh–Plesset equation (Bergmann *et al.* 2006; Ilinskii *et al.* 2012)

$$\frac{d}{dt}(R\dot{R}) \log\left[\frac{R_\infty}{R}\right] - \frac{1}{2}\dot{R}^2 + \frac{p_{V,0} - p_V(t)}{\rho_L} = 0, \quad (4.3)$$

which can be derived by integrating the axisymmetric, incompressible Euler equations from a point far away at a radial distance R_∞ , where the velocity is assumed to be negligibly small, to a point on the bubble surface $R(t)$, using a flow field that obeys the continuity condition $v_r(r) = R\dot{R}/r$. Here, $\dot{R} = dR/dt$ denotes the time derivative of the bubble radius $R(t)$ and $p_V(t)$ is the pressure inside the bubble. Note that viscous and capillary effects can be included straightforwardly into (4.3) by adding the terms $+2\nu_L\dot{R}/R$ and $+\sigma/(\rho_L R)$ on the left-hand side of (4.3), respectively, where ν_L and σ are the water kinematic viscosity and the surface tension of the water–vapour interface. Given the large Reynolds and Weber numbers of the problem we study, where with initial conditions $R_0 > 1.0$ cm, $|\dot{R}_0| > 1.0$ m s^{−1} we find that $Re_0 = |\dot{R}_0|R_0/\nu_L > 10^4$ and $We_0 = \rho_L\dot{R}_0^2R_0/\sigma > 10^2$, we chose to neglect them here to not unnecessarily complicate the description. (Using the fact that $R(t) \sim (t_{coll} - t)^{0.5}$ for the collapse of the hemicylindrical bubble, one may easily verify that $Re(t) \approx Re_0$ and $We(t) \sim We_0(t_{coll} - t)^{-0.5}$, i.e. the local Re is approximately constant and We diverges during collapse.)

Finally, we need a closure that relates the unknown quantity in (4.2), namely $(\partial T/\partial r)_{r=R}$ in the liquid, to the other variables of the problem. The easiest way of formulating such a closure is to just write

$$\left. \frac{\partial T}{\partial r} \right|_{r=R(t)} \approx -\frac{T_V - T_0}{\sqrt{\pi\alpha_L t}}, \quad (4.4)$$

where we divide the temperature difference $\Delta T = T_V - T_0$ between the vapour bubble and the liquid far away from the bubble by a thermal boundary layer thickness $\delta_{th} = \sqrt{\pi\alpha_L t}$ that starts growing at the moment the vapour bubble is entrapped at $t = 0$. Note that $\alpha_L = k_L/(\rho_L c_{p,L})$ is the thermal diffusivity of the liquid. Such an approach would be analytically correct in the limit of a constant temperature difference and for thin thermal boundary layers ($\delta_{th} \ll R(t)$). Whereas the second condition is probably satisfied during most of the time evolution of the bubble, the first most certainly is not, and therefore, (4.4) can be a crude approximation at most. Fortunately, there is an approach that was proposed for the three-dimensional case by Plesset and Zwick (Plesset & Zwick 1952), who formulated an integral equation relating ΔT to $(\partial T/\partial r)_{r=R}$ by formally integrating the spherically symmetric convective heat equation in the limit of a thin thermal boundary

layer, an algebraically quite complex analysis that can, however, straightforwardly be reformulated for the axisymmetric case (Appendix E), leading to

$$T_V - T_0 = -\sqrt{\frac{\alpha_L}{\pi}} \int_{s=0}^t \frac{R(s) \left. \frac{\partial T}{\partial r} \right|_{r=R(s)}}{\sqrt{\int_{w=s}^t R(w)^2 dw}} ds. \quad (4.5)$$

4.2. Results from the vapour bubble collapse model

The set of equations (4.2), (4.3) and (4.5) can be solved numerically, using the appropriate initial value conditions for the wave impact problem studied here, given by

$$R(0) = R_0; \quad \dot{R}(0) = -V_0; \quad p_V(0) = p_{V,0} + \rho_L V_{wave}^2. \quad (4.6)$$

Here, R_0 and V_0 are obtained by determining the time evolution of the cross-sectional area $S(t)$ of the entrapped vapour bubble, where R_0 is the effective radius of the entrapped bubble at the moment of impact, i.e. when it becomes entrapped, defined as $R_0 = \sqrt{2S(t_{impact})/\pi}$, consistent with the approximately hemicylindrical shape of the bubble, and V_0 is determined from the time rate of change of the cavity as $V_0 = -\dot{S}/\sqrt{2\pi S}$, also determined at t_{impact} . The final condition follows from the fact that the bubble is also pressurised by the water mass moving towards the wall. Although the wave impact is a highly unsteady process, the dynamics of the entrapped bubble are likely to be fast as compared with the overall pressurising motion of the wave towards the wall, such that we model it as the constant pressure inside a steady jet of velocity v_{jet} hitting a wall, namely $p_{jet} = \rho_L v_{jet}^2$. If V_{wave} is defined as the average horizontal velocity in the neighbourhood of the cavity, one may consequently estimate the pressure as $\Delta p_{rise} \approx \rho_L V_{wave}^2$. The way in which these quantities are measured from the movies and the resulting values are further discussed in Appendix B, where we also argue that the inertial pressure scale is the appropriate scale to take.

Regarding V_0 and V_{wave} it is worth noting that, although they are caused by the same physical phenomenon and have a similar magnitude, they are nevertheless causing distinctly different effects, that each of them separately may cause a cavity to collapse: if a quiescent cavity is created inside a liquid at a slightly higher pressure than the equilibrium vapour pressure, it will cause the cavity to shrink. If on the other hand a cavity is present in a liquid at equilibrium pressure but the cavity walls are given an initial inward velocity, the cavity will continue to shrink due to the converging action of the inertia present in the surrounding liquid. The first effect is connected to a diffuse, undirected pressure rise inside the liquid as a whole, whereas the second is the result of the already existing converging motion of the liquid.

Taking the case $\alpha = 0.385$, we find from the experiment that $R_0 \approx 2.45$ cm, $V_0 \approx 1.8$ m s⁻¹ and $V_{wave} \approx 1.7$ m s⁻¹ (Appendix B). In figure 10(a) we plot the bubble radius as a function of time, as obtained by the solution of the model system for four different values of the temperature T_0 . Here we observe that, for the lowest temperature ($T_0 = 20$ °C), there is a full collapse of the vapour bubble. For $T_0 = 40$ °C, the bubble almost fully collapses but subsequently rebounds, whereas for the largest two temperatures ($T_0 = 60$ and 80 °C), the bubble appears to perform a damped oscillation. It is good to note that the latter is not due to viscous dissipation in the liquid phase, since this is neglected in (4.3), and of course also would be way too small to cause such a substantial dissipation. Instead, it is connected to condensation/evaporation cycles, where heat needs to respectively be stored in and retracted from the liquid.

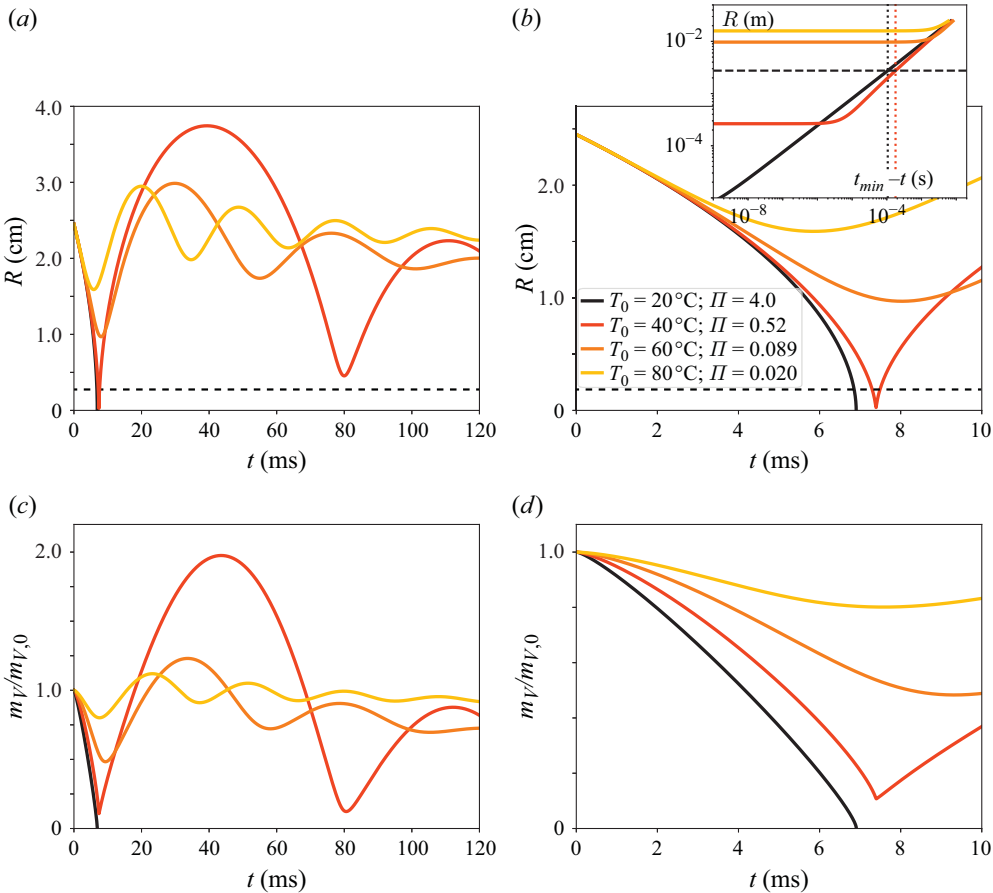


Figure 10. Solution of the model system using the parameters observed for a wave of steepness $\alpha = 0.385$ ($R_0 \approx 2.45$ cm, $V_0 \approx 1.8$ m s $^{-1}$ and $V_{wave} \approx 1.7$ m s $^{-1}$) and $R_\infty = W = 0.60$ m. (a) The vapour bubble radius $R(t)$ as a function of time t for four different temperatures, $T = 20, 40, 60$ and 80 °C. The horizontal dashed line indicates the radius of the pressure sensors used, $R_{sensor} = 2.75$ mm. (b) Same data as in (a) but zoomed in on the region until the first minimum occurs. The inset shows the same radius data but now as a function of the time $t_{min} - t$ remaining until the first minimum is reached, in a doubly logarithmic plot. (c) The corresponding vapour mass $m_V(t)$ divided by the original mass present in the bubble $m_{v,0} = m_V(0)$, again as a function of time t . (d) Same data as in (c) but zoomed in.

Zooming in on the first 10 ms of the collapse (figure 10b) it is clear that at first all bubbles follow the same path, which of course can be traced back to V_0 and V_{wave} being the same in all cases, but soon the lowest temperature bubble appears as the fastest. Nevertheless, it is not the first to reach a minimum, which in fact is the highest temperature bubble. The $T_0 = 20$ °C bubble collapses as if no vapour was present in the bubble and the curve virtually overlaps with the one from an empty cavity using the same initial conditions, condensing all vapour present in the bubble in the process. The $T_0 = 40$ °C bubble collapses to an almost negligible radius of $R_{min} = 260$ μ m, corresponding to 0.011 % of the original volume, but as can be seen in the corresponding time evolution of the vapour mass in figures 10(c) and 10(d), defined as the product of the bubble volume and density, $m_V(t) = (1/2)\pi W R(t)^2 \rho_V(t)$, the minimum vapour mass is still substantial, at about 10 % of its initial value, and consequently, pressure and density at the minimum are high.

The two largest temperature bubbles however do not collapse but oscillate. The one at $T_0 = 60\text{ }^\circ\text{C}$ reaches its first minimum even slightly after the $40\text{ }^\circ\text{C}$ one, but that of $T_0 = 80\text{ }^\circ\text{C}$ even before the lowest temperature bubble has collapsed. This is remarkable, but can be traced back to the fact that these highest temperature bubbles oscillate very similar to a gas bubble, at an equilibrium pressure equal to $p_{V,0} + \rho_L V_{wave}^2$, which is highest for the $80\text{ }^\circ\text{C}$ one and, therefore, leads to the largest oscillation frequency, i.e. the smallest period. Finally, comparing the time at which the minimum radius is reached with that at which the vapour mass is minimal, there is a clear shift: the minimum in the vapour mass is reached later than the minimum in radius. This can be traced back to the behaviour of the thermal boundary layer: as the minimum radius is reached, the vapour temperature becomes maximal and there is a thermal boundary layer transporting condensation heat into the liquid. This continues as the bubble starts to expand because the vapour temperature will still be higher than the far-field liquid temperature T_0 . In principle this could continue until the vapour temperature becomes equal to T_0 , but due to the fact that in the Plesset–Zwick formula the history of the thermal boundary layer is taken into account, this will happen earlier. The phase shift between the time evolution of the bubble and the structure of the thermal boundary layer in the liquid is ultimately also responsible for the damping of the oscillation.

Figure 11(a,b) shows the pressure $p_V(t)$ inside the vapour bubble as a function of time, again for the four ambient temperatures considered in figure 10. For the lowest two temperatures, the model pressures can reach highly unphysical values of thousands of bar (not shown), which are well beyond the critical point of water at $p = 220.64\text{ bar}$, where the difference between vapour and liquid disappears and the model has lost its validity. For the highest temperatures, the vapour pressure remains very moderate with values of the order of 1 bar maximally. This is also true for the first rebound of the $T_0 = 40\text{ }^\circ\text{C}$ case, where the maximum pressure equals 0.3 bar.

Clearly, the computed vapour pressure would be only then equal to what is measured with the pressure sensors that we are using in the experiments, if the sensor is completely immersed inside the vapour bubble. As soon as the pressure sensor is partly covered by vapour and partly by liquid, the situation changes as sketched in figure 9(b) and more care needs to be taken. This case is treated in Appendix F, where an expression for the average pressure on the sensor area p_{sensor} is derived, which is subsequently reported in figure 11(c,d), where we also take into consideration that the sensor has a finite response time of $\approx 5\text{ }\mu\text{s}$ (corresponding to the 200 kHz acquisition rate), such that we report a time average over $5\text{ }\mu\text{s}$. Here, we see that the maximum pressures reached on the sensor area for the lowest two temperatures are of the order of 100 bar, i.e. of the same order as those measured in the experiment, especially for the $40\text{ }^\circ\text{C}$ case. For the higher temperatures, the sensor pressure is equal to the vapour pressure, as expected.

At this point it is good to ask how much of the observed high pressures in the model at lower temperatures are due to condensation and how much is just due to the fact that the equilibrium vapour pressure rapidly decreases with temperature? Clearly, also an adiabatic compression model would predict an increase of the pressure in the vapour pocket at lower ambient vapour pressures. Therefore, we numerically solved the Rayleigh–Plesset equation (4.3) with an adiabatic model for the vapour in the pocket (i.e. excluding phase change) and compared the result with the phase-change model presented in this section, using the same input parameters in both cases. The results, which are presented in more detail for the case $\alpha = 0.385$ in Appendix G, show that indeed there is a small effect, raising the pressure from 0.62 bar at $T_0 = 70\text{ }^\circ\text{C}$ to 2.46 bar at $T_0 = 20\text{ }^\circ\text{C}$. Evidently, this effect is small and is dwarfed by the very large pressures ($\sim 100\text{ bar}$) predicted by the phase-change model.

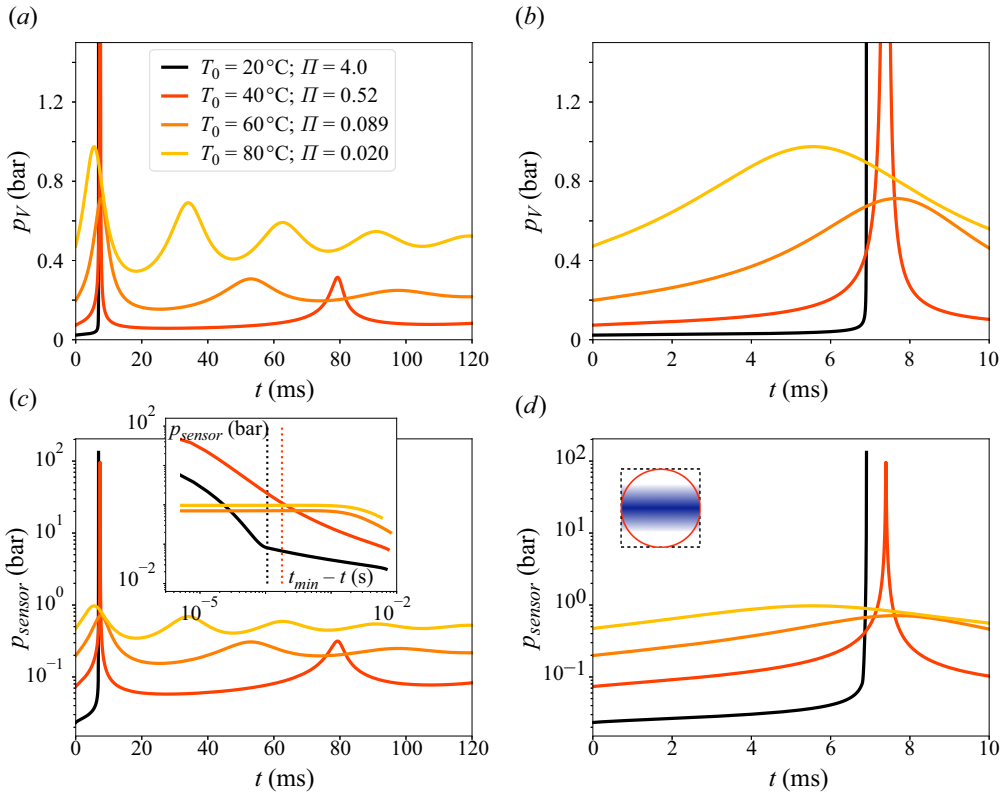


Figure 11. Pressures in the model system using the same parameters as used in figure 10. (a) The vapour pressure $p_V(t)$ as a function of time t . (b) Same data as in (a) but zoomed in on the region until the first minimum occurs. (c) The pressure $p_{sensor}(t)$ averaged over the sensor area and response period, again as a function of time t . (d) Same data as in (c) but zoomed in. The inset in (c) shows the increase of p_{sensor} towards the first minimum in R (corresponding to the first maximum in p_V) in a doubly logarithmic plot. Note that in the experiment one may expect the sensor to measure $P_{sensor} = p_{sensor} - p_{V,0}$ rather than p_{sensor} itself. The inset in (d) shows a sketch of the pressure intensity (blue) on the sensor when the bubble radius is smaller than the sensor radius. The dashed square indicates the region taken to determine an estimate for the measured pressure in Appendix F. Note that in this theoretical figure absolute pressures are reported (in contrast to the gauge pressures of the experimental figures) to better separate the curves corresponding to different temperatures from one another.

Finally, although in certain aspects the model agrees reasonably well with the experiments, there are clear dissimilarities as well. The most obvious ones have to do with the surface instabilities that occur on the surface of the vapour pocket, which essentially causes it to break up into a large bubble cloud rather than a single bubble after the first compression. This is clearly not captured by the model and will cause even more dissipation during oscillations. Nevertheless, the main features of the dynamics connected to phase change appear to be reasonably well captured.

4.3. Non-dimensionalisation of the model

To obtain additional insight, we non-dimensionalise the model of (4.2), (4.3) and (4.5) using the initial bubble radius R_0 as the length scale, the initial velocity $-V_0$ as the velocity scale and the equilibrium values $p_{V,0}$, $\rho_{V,0}$ and T_0 as reference scales for the thermodynamic state variables. This leads to $\tilde{R} = R/R_0$, $\tilde{t} = V_0 t/R_0$, $\tilde{R} = \dot{R}/V_0$ (where

for the dimensionless case the dot is understood to indicate a derivative with respect to dimensionless time \tilde{t} , $\tilde{p}_V = p_V/p_{V,0}$, $\tilde{\rho}_V = \rho_V/\rho_{V,0}$ and $\tilde{T}_V = T_V/T_0$. In addition, to simplify the discussion we use the approximate expression (4.4) for the temperature gradient at the bubble interface. The same conclusions can be drawn from the full set of equations, but the analysis is obscured by the complexity of (4.5).

The non-dimensionalised set of equations becomes

$$\left(\frac{d}{d\tilde{t}}(\tilde{R}\dot{\tilde{R}})\right) \log\left[\frac{\tilde{R}_\infty}{\tilde{R}}\right] - \frac{1}{2}\dot{\tilde{R}}^2 - \frac{\tilde{p}_V - 1}{Eu_0} = 0, \tag{4.7a}$$

$$\frac{d\tilde{p}_V}{d\tilde{t}} = 2\left(\frac{\partial\tilde{\rho}_V}{\partial\tilde{p}_V}\right)^{-1} \left[-\tilde{\rho}_V\frac{\dot{\tilde{R}}}{\tilde{R}} - \Lambda\frac{\tilde{T}_V - 1}{\tilde{R}\sqrt{\tilde{t}}}\right], \tag{4.7b}$$

with initial conditions

$$\tilde{R}(0) = 1, \quad \dot{\tilde{R}}(0) = -1, \quad \tilde{p}_V(0) = 1 + Eu_{wave}, \tag{4.8}$$

where we have defined the dimensionless groups

$$Eu_0 = \frac{\rho_L V_0^2}{p_{V,0}}, \quad Eu_{wave} = \frac{\rho_L V_{wave}^2}{p_{V,0}}, \quad \Lambda = \frac{k_L T_0}{\rho_{V,0} L \sqrt{\pi \alpha_L R_0 V_0}} = \frac{\beta}{\sqrt{\pi}} \frac{\rho_L}{\rho_{V,0}} \frac{c_{p,L}}{\mathcal{R}_s} \sqrt{\frac{\alpha_L}{R_0 V_0}}. \tag{4.9}$$

The first two groups represent Euler numbers based on the velocity scales V_0 and V_{wave} , respectively, whereas the last one contains $\beta = \mathcal{R}_s T_0/L$, the Péclet number $Pe^{-1/2} = (R_0 V_0/\alpha_L)^{-1/2}$, the density ratio $\rho_L/\rho_{V,0}$ of liquid and vapour and the ratio of the specific heat of the liquid and the specific gas constant of the vapour, $c_{p,L}/\mathcal{R}_s$.

By construction, all the dimensionless variables in (4.7) (namely \tilde{R} , $\dot{\tilde{R}}$, \tilde{p}_V and \tilde{T}_V) are of order unity, at least shortly after the beginning of the dynamics, close to $t = 0$. Note that, for our experiments, since the Euler numbers are typically (considerably) smaller than 1, the initial condition for the pressure (4.8) is also of order one. This implies that we need to give special attention to the terms $\tilde{p}_V - 1$ and $\tilde{T}_V - 1$ in (4.7). Starting with the last one we may estimate

$$\tilde{T}_V - 1 = \frac{T_V - T_0}{T_0} \approx \beta \frac{p_V - p_{V,0}}{p_{V,0}} = \beta(\tilde{p}_V - 1), \tag{4.10}$$

where we have used the linearised Clausius–Clapeyron relation (C4). For the term $\tilde{p}_V - 1$, one may estimate

$$\tilde{p}_V - 1 \sim \tilde{p}_V(0) - 1 = \frac{p_V(0) - p_{V,0}}{p_{V,0}} = \frac{\rho_L V_{wave}^2}{p_{V,0}} = Eu_{wave} \sim Eu_0, \tag{4.11}$$

such that a new order-one variable $\tilde{\Delta}$ can be introduced to replace $\tilde{p}_V - 1$ as

$$\tilde{\Delta} \equiv \frac{\tilde{p}_V - 1}{Eu_0}. \tag{4.12}$$

With this definition our set of equations with initial conditions becomes

$$\left(\frac{d}{d\tilde{t}}\left(\tilde{R}\dot{\tilde{R}}\right)\right)\log\left[\frac{\tilde{R}_\infty}{\tilde{R}}\right]-\frac{1}{2}\dot{\tilde{R}}^2-\tilde{\Delta}=0, \quad (4.13a)$$

$$\frac{d\tilde{\Delta}}{d\tilde{t}}\approx\frac{2}{Eu_0}\left(\frac{\partial\tilde{\rho}_V}{\partial\tilde{p}_V}\right)^{-1}\left[-\tilde{\rho}_V\frac{\dot{\tilde{R}}}{\tilde{R}}-\Pi\frac{\tilde{\Delta}}{\tilde{R}\sqrt{\tilde{t}}}\right], \quad (4.13b)$$

$$\tilde{R}(0)=1, \quad \dot{\tilde{R}}(0)=-1, \quad \tilde{\Delta}(0)=\frac{Eu_{wave}}{Eu_0}=\left(\frac{V_{wave}}{V_0}\right)^2\equiv\kappa, \quad (4.13c)$$

where the term $\partial\tilde{\rho}_V/\partial\tilde{p}_V=\tilde{\rho}_V/\tilde{p}_V-\beta\approx 1$, using (C5), could be further simplified. With respect to our discussion below (4.2), there is one key dimensionless parameter in this set of equations that determines the quality of the behaviour of the vapour bubble, namely Π , defined as

$$\Pi=\beta\Lambda Eu_0=\frac{\beta^2}{\sqrt{\pi}}\frac{\rho_L}{\rho_{V,0}}\frac{c_{p,L}}{\mathcal{R}_s}Pe^{-1/2}Eu_0. \quad (4.14)$$

If $\Pi\gg 1$, the second term in the dimensionless energy-mass balance equation is dominant, and a violent vapour bubble collapse is expected, similar to that predicted from the Rayleigh equation for an empty cavity. For the examples provided in figures 10 and 11, this would correspond to the $T_0=20^\circ$ case, for which $\Pi=4.0$. The second-lowest temperature ($T_0=40^\circ\text{C}$) is with $\Pi=0.52$ in the crossover region, whereas the two highest temperatures ($T_0=60$ and 80°C), for which $\Pi=0.089$ and 0.020 , respectively, are in the region where oscillations of the vapour bubble are dominant, similar to those of an oscillating non-condensable gas bubble that is entrapped during impact.

The other two dimensionless parameters in (4.13), namely Eu_0 , which has influence on the overall time scale but not on the balance between the two terms on the right-hand side of (4.13b), and the order-one parameter $\kappa=V_{wave}^2/V_0^2$, which appears in the initial value for the pressure variable $\tilde{\Delta}$ in (4.13c), are of smaller (although not negligible) consequence for the dynamics of the vapour bubble.

4.4. Measured maximum pressures in the light of model results

Now that we have identified a single dimensionless parameter, Π , to characterise the qualitative behaviour of the entrapped vapour bubble, we may use this knowledge to re-examine the maximum vapour pocket collapse pressure data from figure 7. To this end, we compute the value of Π for each temperature and wave steepness and plot the result in the inset of figure 12. In this doubly logarithmic plot, we see, for each α separately, that the data shows the behaviour we expect: for small values ($\Pi\ll 1$), the measured average maximum vapour pocket pressure $\langle P_{pocket}\rangle$ is small, of the order of 0.1–1 bar, connected to a relatively small amount of condensation (or evaporation) and close to non-condensable gas pocket behaviour, whereas for intermediate values ($\Pi\sim 1$), the pressures suddenly rise until, for large values ($\Pi\gg 1$), we find that the very large pressures connected to a full vapour pocket collapse, in the regime where the latent heat of condensation can be easily transported into the liquid. The intermediate region is clearly visible for $\alpha=0.385$, whereas the vapour pocket collapse region is particularly strong for $\alpha=0.35$ and the small pressure response is dominant for $\alpha=0.42$. Unfortunately, the data for the three wave steepnesses seem shifted with respect to one another, such that the data collapse of the plot is unsatisfactory. Let us now look into the origin of this discrepancy. Note that Π decreases monotonically, but nonlinearly with temperature.

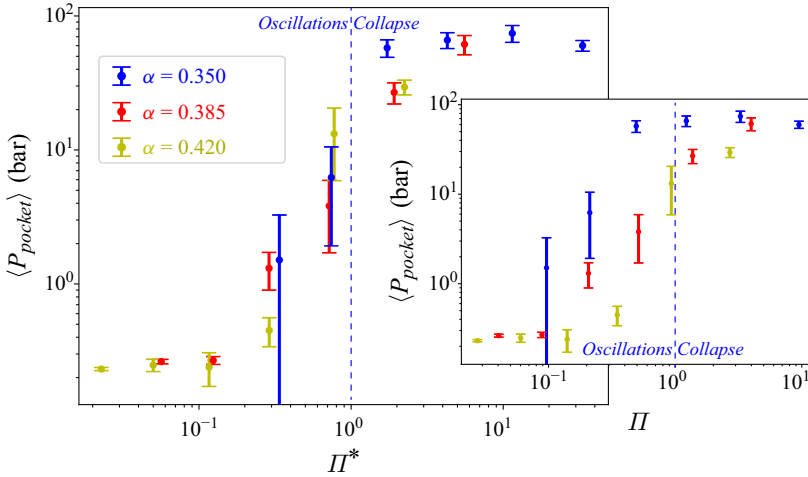


Figure 12. Average maximum vapour pocket pressure $\langle P_{pocket} \rangle$ data for all three investigated wave shapes $\alpha = 0.35$ (blue), 0.385 (red) and 0.42 (yellow), i.e. the same data as plotted in figure 7. When the data are plotted as a function of the key dimensionless parameter Π , which characterises the qualitative behaviour of the entrapped vapour bubble, the data collapse between the different wave steepnesses α is unsatisfactory (inset), but when the modified parameter Π^* is used the data collapse is convincing (main plot). As in figure 7, the symbols represent the average over the individual experiments (data not shown), and the error bars are twice the standard deviation of the sample and would be symmetric on a linear scale. The vertical dashed blue lines indicate the condition $\Pi = 1$ (and $\Pi^* = 1$), marking the boundary between the regions in which non-condensable gas-like behaviour (oscillations, $\Pi, \Pi^* < 1$) and vapour-like behaviour (collapse, $\Pi, \Pi^* > 1$) is expected.

The first cause is the fact that the entrapped vapour pockets are assumed to be hemicylindrical, whereas in fact they are rather flattened, especially in the case of small α . This means that the thermal contact in the experiment is larger than in the model. It is in fact straightforward to evaluate the consequences, if $\ell(t)$ is the measured wetted length of the vapour pocket, and $S(t) = (1/2)R_{eff}^2$ is its cross-sectional area, then we can write the energy-mass balance (4.1), with $m_V = S(t)W\rho_V(t)$, as

$$\frac{1}{2}\pi R_{eff}^2 \frac{d\rho_V}{dt} = -\pi R_{eff} \dot{R}_{eff} - \frac{k_L \ell}{L} \left. \frac{\partial T}{\partial n} \right|_{\partial S}, \tag{4.15}$$

where $\partial T/\partial n$ is the normal derivative at the liquid–vapour interface ∂S . Writing this equation in the form of (4.2) we obtain

$$\left(\frac{\partial \rho_V}{\partial p_V} \right) \frac{dp_V}{dt} = -2\rho_V \frac{\dot{R}_{eff}}{R_{eff}} + \frac{2k_L}{LR_{eff}} \left[\frac{\ell}{\pi R_{eff}} \right] \left. \frac{\partial T}{\partial n} \right|_{\partial S}. \tag{4.16}$$

Note that if one replaces R_{eff} by R , we exactly retrieve (4.2), with the exception of the factor between square brackets in the second term, $\ell/(\pi R_{eff}) = \ell/\sqrt{2\pi S}$, which multiplies the heat flux, and in the process of non-dimensionalisation leads to an additional multiplicative factor $\ell/(\pi R_{eff})$ in Π , that is not present in the analysis of the previous subsection. Here, it is good to note that the multiplication factor represents the ratio of the wetted length to that of a hemicylindrical cavity of the same area.

The second cause is due to the presence of κ in the initial value condition (4.13c) on the pressure variable $\tilde{\Delta}$. If we compare our experiments to the ideal case $\kappa = 1$, corresponding to $V_{wave} = V_0$, then we see that in the first stages of the dynamics $\tilde{\Delta}(t) \sim \kappa$, i.e. different

from 1. To at least initially regauge the dynamics to the $\kappa = 1$ case, we may simply introduce an effective value for Π by dividing Π by κ .

Consequently, if we introduce a modified version Π^* of our key parameter, defined as

$$\Pi^* \equiv \frac{1}{\kappa} \frac{\ell_0}{\pi R_{eff,0}} \Pi, \quad (4.17)$$

we may hope for a better collapse of the data. And, indeed, this is corroborated from our experimental data, when looking at the very good collapse of the data in the main figure of [figure 12](#), where we plot $\langle P_{pocket} \rangle$ as a function of Π^* as defined in (4.17). Note that the subscript 0 in ℓ_0 and $R_{eff,0}$ indicate that these quantities are evaluated at the impact time t_{impact} .

In conclusion, the model defined in this section is capable of capturing the essential physics of breaking wave impact in a boiling liquid. This is remarkable, since the large scale of the dynamics creates many additional dynamics already during vapour pocket compression or collapse, such as the development of surface instabilities; and definitely after reaching the first minimum, where the vapour pocket has broken up into a bubble cloud, the dynamics is expected to be significantly different. Also, even when taking utmost care in controlling the pressure inside the autoclave, we cannot exclude the presence of small amounts of non-condensable gases (air), especially that dissolved into the liquid phase, that may alter the dynamics of our system, e.g. in the form of small gaseous bubbles that may act as nuclei for vapour bubbles in the rarefaction stage that follows a complete collapse and will cause a secondary vapour bubble cloud to be created and collapse, forming the observed rebound.

Finally, since the data collapse observed in [figure 12](#) is the result of dimensional analysis, one may argue that also the average maximum vapour pocket pressure $\langle P_{pocket} \rangle$ needs to be non-dimensionalised, most specifically using the vapour pressure $p_{V,0}$. This, however, is only applicable for pressures smaller than a few bar, since the larger ones are all diverging and, therefore, crucially determined by the finite sensor size and response time (cf. the integration procedure outlined in [Appendix F](#)). These additional scales do interfere with the theoretically expected pressure scaling, but do not interfere with the qualitative behaviour of the vapour pocket, which is solely determined by the value of Π (or Π^*), as becomes clear from (4.13b). As a consequence, the value of $\langle P_{pocket} \rangle$ is a good measure of this qualitative behaviour.

5. Discussion and conclusion

To summarise the findings in this work, we performed large-scale wave impact experiments in water and water vapour under boiling liquid conditions, that is, where water and vapour are in thermodynamic equilibrium at a controlled temperature on the vapour curve. We used the ATM facility at MARIN, in which the equilibrium temperature was varied from 20 °C to 70 °C in steps of 10 °C. The waves were produced as solitons by a single stroke of a wavemaker in a flume contained inside the setup, which were subsequently turned into breaking waves by a slope immersed in the flume. We used waves with three different steepnesses ($\alpha = 0.35, 0.385$ and 0.42), where the main difference lies in the size of the entrapped vapour pocket that increases nonlinearly with α , and the secondary difference is formed by the rate at which it is compressed.

Our main experimental findings are that pressures occurring during the impact of a wave under boiling liquid conditions can be up to two orders of magnitude larger than those in comparable wave impacts of water in air. This can be traced back to the very large pressures occurring during collapse of the vapour pocket. We created a simplified model,

Property	Units	H ₂ O at 20 °C	H ₂ O at 100 °C	LNG	LH2
ρ_L	kg m ⁻³	998	958	423	70.4
α_L	mm ² s ⁻¹	0.14	0.17	0.12	0.14
T_0	K	293	373	112	20.4
$p_{V,0}$	bar	0.023	1.01	1.01	1.01
L	MJ kg ⁻¹	2.45	2.26	0.51	0.45
$\rho_L/\rho_{V,0}$	1	5.8×10^4	1.6×10^3	244	59.2
$c_{p,L}/\mathcal{R}_s$	1	9.1	9.1	6.8	2.4
β	1	0.05	0.08	0.11	0.19
$\Pi_{1,1}$	s ^{3/2} m ⁻¹	0.15	1.9×10^{-4}	1.8×10^{-5}	7.3×10^{-7}

Table 1. Relevant transport properties and dimensionless groups for water at 20 °C and 100 °C, LNG and liquid hydrogen (LH2). Tabulated are the liquid density ρ_L , liquid thermal diffusivity α_L , equilibrium temperature T_0 , equilibrium vapour pressure $p_{V,0}$ and latent heat L . These are followed by the liquid to vapour density ratio $\rho_L/\rho_{V,0}$, the ratio of the liquid isobaric specific heat and the vapour specific gas constant $c_{p,L}/\mathcal{R}_s$, the parameter $\beta = \mathcal{R}_s T_0/L$ and finally the quantity $\Pi_{1,1}$ introduced in the text.

treating the vapour pocket as a hemicylinder, that is in reasonably good agreement with the experiments. From this model we distilled a single dimensionless parameter, Π , the value of which determines the character of the vapour pocket dynamics. If $\Pi < 1$ then vapour cannot sufficiently condense and the dynamics resemble the oscillations of a non-condensable gas bubble, but more strongly damped, whereas if $\Pi > 1$, the condensation heat can be efficiently transported into the liquid leading to a collapsing vapour bubble. The two regimes are clearly visible in our experiment, and can be classified using the value of Π , or rather its modified version Π^* .

A secondary experimental finding is that the pressures exerted during the impact of the crest at boiling liquid conditions appear to be slightly larger than those experienced during a similar wave impact in air. Due to the fact that the effect on the pressure is maximally a factor of 2, i.e. much smaller than that in the vapour pocket, this observation has not been investigated in greater detail and would call for further study.

The fact that the dynamics of a vapour pocket can be classified using Π allows us to evaluate whether vapour bubble collapse could occur in the industrially relevant case of transport of cryogenic liquids. To that end, in [table 1](#) we summarise values of some key transport properties and dimensionless groups occurring in Π for LNG and liquid hydrogen (LH2), where for definiteness, we use the boiling point under atmospheric conditions, which for LNG is one of the most common ways in which it is transported overseas. For comparison, we also provide the corresponding values for water at its boiling point, together with the lowest temperature used in our experiments, $T_0 = 20$ °C. It should also be noted that a similar derivation can be made for spherically symmetric bubbles entrapped in the liquid, provided in [Appendix H](#), which leads to exactly the same form of Π , such that this discussion is not limited to axisymmetrically collapsing cylindrical bubbles.

Once the thermal equilibrium state is set, the two control parameters that remain in Π are the bubble radius R_0 and the velocity scale V_0 . Noting that these values are contained in the Péclet and Euler numbers, $Pe = R_0 V_0/\alpha_L$ and $Eu_0 = \rho_L V_0^2/p_{V,0}$, we may rewrite the definition (4.14) as

$$\Pi = \frac{\beta^2}{\sqrt{\pi}} \frac{\rho_L}{\rho_{V,0}} \frac{c_{p,L}}{\mathcal{R}_s} \frac{\rho_L \sqrt{\alpha_L}}{p_{V,0}} R_0^{-1/2} V_0^{3/2} \equiv \Pi_{1,1} R_0^{-1/2} V_0^{3/2}. \quad (5.1)$$

Clearly, Π increases when the velocity scale V_0 increases, but also when the bubble radius R_0 decreases. The first can be traced back to the driving force, namely the pressure

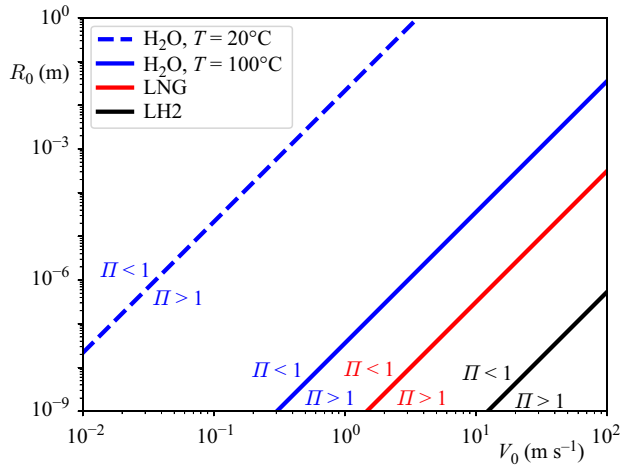


Figure 13. Phase diagram showing the condition $\Pi = 1$ for the main control parameters bubble radius R_0 and velocity V_0 along the vertical and horizontal axis, respectively, for water at room temperature (20 °C, dashed blue line), water at 100 °C (blue line), LNG (red line) and liquid hydrogen (LH2, black line), all three at their respective boiling points. For each line, the region to the top left of it is where $\Pi < 1$ and non-condensable gas-bubble-like oscillations are expected, whereas the region to the bottom right is where collapsing bubbles are expected.

difference (and therefore temperature difference) between vapour and liquid, becoming larger and the second one to the area-to-volume ratio becoming larger, which makes heat transport of the condensation heat into the liquid easier. In figure 13 we now plot, for the four substances discussed above, the transitional condition $\Pi = 1$, or, with (5.1),

$$R_0 = \Pi_{1,1}^2 V_0^3. \tag{5.2}$$

These demarcation curves appear as straight lines in the doubly logarithmic plot, and the region to the top left of each plot corresponds to relatively benign oscillations, whereas the region to the bottom right corresponds to violent collapse. Furthest to the left is the demarcation line for water and vapour at an equilibrium temperature of $T_0 = 20$ °C, which lies in the middle of the region of interest for wave impact on a large, industrial scale, with radii of the order of decimetres and metres and velocities of the order of 10 m s^{-1} . However, the demarcation line for water at its boiling temperature lies considerably to the right, that of LNG further to the right and LH2 even further to the right. This implies that as long as vapour bubbles are large and compact (i.e. close to spherical or cylindrical), there is little risk for a violent collapse as observed during our relatively low-temperature experiments, except for very small bubbles. This statement is already true for water and vapour at its boiling point, but even more true for LNG and LH2.

We can also see from our experiments, however, that shape plays an important role, and that the differences as observed in the inset of figure 12, where the non-spherical bubbles corresponding to $\alpha = 0.35$ cause collapse already at relatively small values of Π , the situation may rapidly change for these non-cylindrical (or non-spherical) bubbles. This suggests that thin layers of vapour, with good thermal contact to the liquid, may be subject to rapid condensation also in the case of LNG and LH2, and certainly need closer investigation.

Finally, there is another way in which a relatively large bubble may be in good thermal contact, and that is when it is present in the form of a bubble cloud, which is known to dynamically behave similarly to a large bubble of similar gas/vapour content, but where the condensation heat can be much more easily transported into the liquid, which may lead

to a violent collapse long before the demarcation line from [figure 13](#). Since such a bubble cloud may easily be formed as a consequence of instabilities that are observed to occur during oscillations or (partial) collapse, this case also deserves further study.

Supplementary material. Supplementary material are available at <https://doi.org/10.1017/jfm.2025.110>.

Acknowledgements. The authors acknowledge many stimulating discussions with A. Prosperetti. In addition, we would like to thank H. Siebers and E. Seves for their technical support.

Funding. This work is part of the Vici project IMBOL (project number 17070), which is partly financed by the Netherlands Organisation for Scientific Research (NWO).

Declaration of interests. The authors report no conflict of interest.

Appendix A. Repeatability of the wave shape

In order to evaluate the repeatability of the wave shape in the experiments, we show in [figure 14](#) the wave shape in the frame just before the impact moment (at $t = t_{impact}$) for all temperature settings T_0 and for all three wave shapes (reflected in the wave steepness α) used in our experiment. Here, we find a good degree of repeatability of the wave crest as a function of T_0 for all three values of α . When inspecting the shape of the vapour pocket that is enclosed below the crest impact point for varying T_0 , we find that there is very good agreement for $\alpha = 0.385$ and $\alpha = 0.420$, but for the smallest vapour pocket ($\alpha = 0.350$), we observe small differences in both shape and volume. This is likely due to the fact that the smallest $\alpha = 0.35$ in our experiments is close to the limit of a flip-through wave (Ezeta *et al.* 2023), where the reproducibility of the wave shape is often found to be challenging, as reported by others (Lugni *et al.* 2006; Hofland *et al.* 2010).

A second observation is that in some cases small vapour bubbles are randomly entrapped along the moving liquid interface, as are visible for $\alpha = 0.385$ at $T_0 = 70$ °C and for $\alpha = 0.420$ at most temperatures. These, however, likely arise from the interaction of the wave with the side wall and are therefore of little consequence to the collapse in the region where the pressure sensors are located, since they do not appear to influence the overall shape of the wave.

To further investigate repeatability, we turn to the least repeatable case, namely $\alpha = 0.35$, and compare the wave shape for all 10 repetitions of the experiment at $T_0 = 20$ °C in [figure 15](#). We may conclude that even for these worst case settings, repeatability is good. Further evidence of the good degree of repeatability is provided in [Appendix B](#), where the wave shape is characterised in greater detail for the individual experiments performed in this study.

Also from a more theoretical perspective, for the density ratios $\rho_L/\rho_{V,0}$ used in this experiment, which are all larger than 10^3 , the effect of the vapour/gas density on the motion of the wave in the flume is expected to be negligible. This has been verified in the experimental setup as well (Ezeta *et al.* 2023).

A final note is that, for each experimental setting, the individual experiment reproduced in [figure 14](#) constitutes an arbitrary selection from the 10 repetitions that have been made for each setting.

Appendix B. Analysis of the shape of the entrapped vapour pocket

From the side view high-speed imaging recording we determine the major wave characteristics that are used in this work. In [figures 16\(a\)–16\(c\)](#) we show snapshots of three wave shapes upon impact. These correspond to three values of α that are explored in

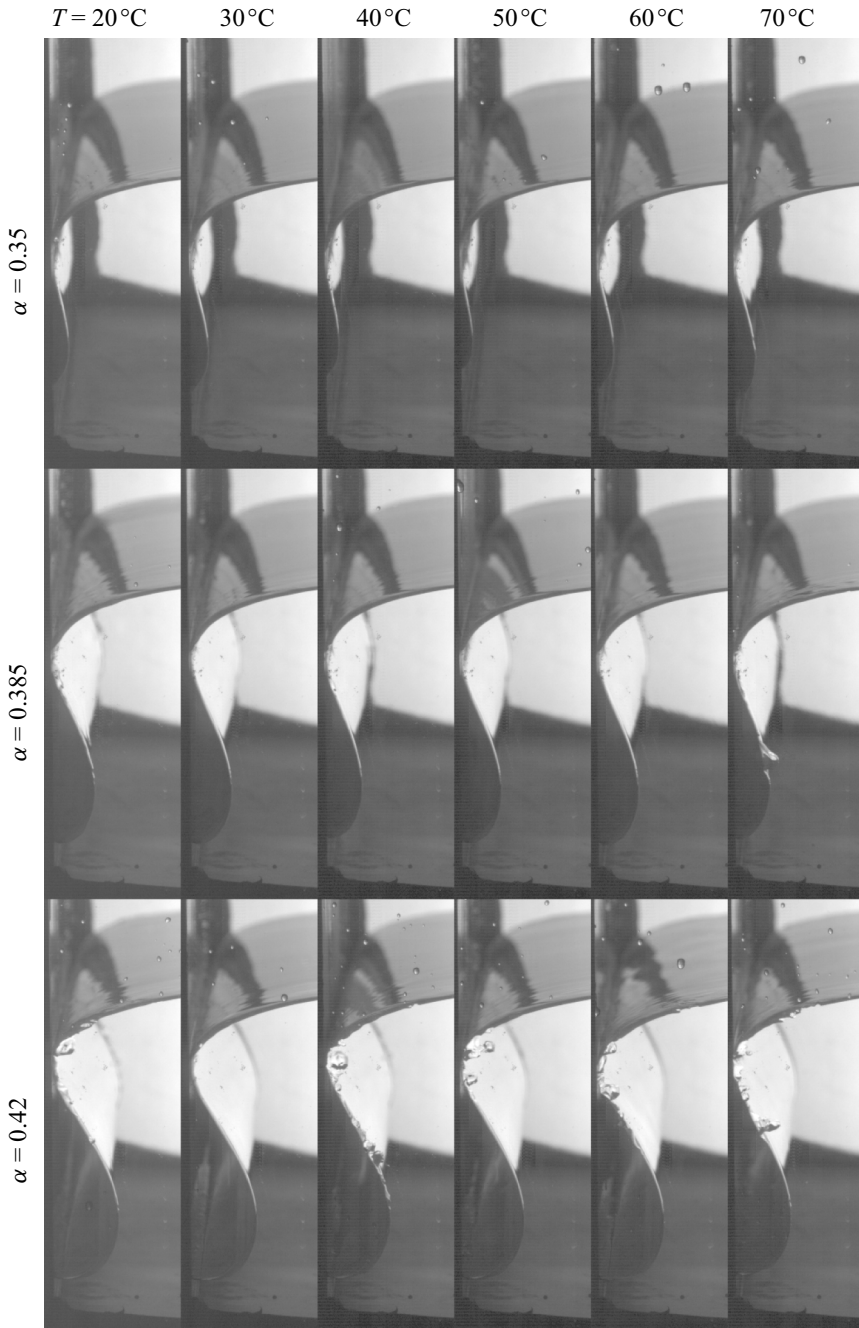


Figure 14. We compare the wave shape in the frame just before impact (at $t = t_{\text{impact}}$) for all settings of the temperature T_0 (horizontal direction) and wave shape (vertical direction) used in the experiment.

this work. For $\alpha = 0.35$, we observe the entrapment of a slender and thin vapour pocket. In contrast, for the largest $\alpha = 0.42$, we find a similar wave shape albeit with a larger curvature at the wave crest and what appears to be a hemicylindrical vapour pocket. Clearly, the shape of the vapour pocket of the intermediate case $\alpha = 0.385$ lies between the two extremes. In [figure 16\(d\)](#) we show how some key wave shape parameters are extracted.

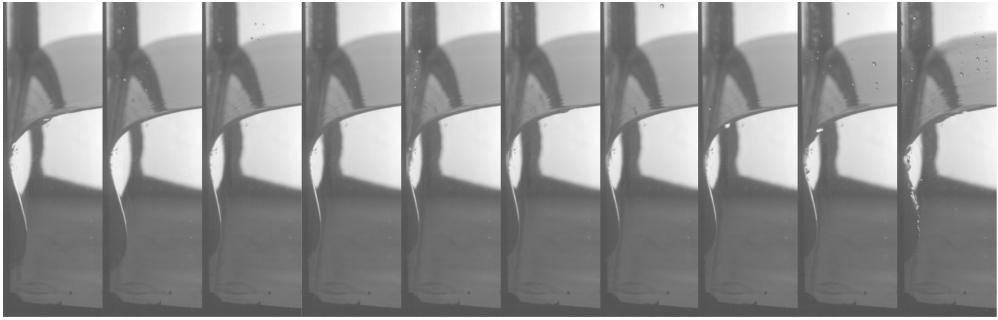


Figure 15. Wave shape just before impact (at $t = t_{\text{impact}}$) for all 10 repetitions of the experiment at $\alpha = 0.35$ and $T_0 = 20\text{ }^\circ\text{C}$, showing the degree of repeatability.

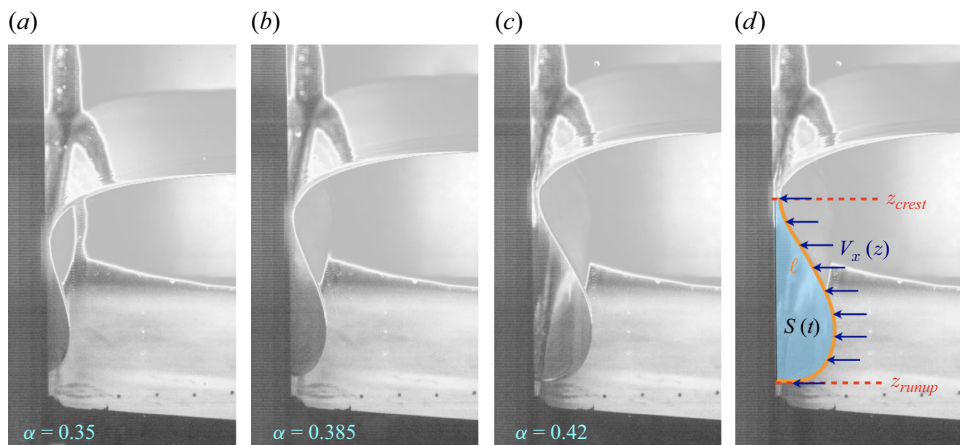


Figure 16. (a,b,c) The three wave shapes used in this experiment, with wave steepness (a) $\alpha = 0.35$, (b) $\alpha = 0.385$ and (c) $\alpha = 0.42$. (d) In the $\alpha = 42$ case we indicate how the surface area $S(t)$ (light blue) and wetted length $\ell(t)$ (orange curve) of the entrapped vapour pocket were determined. Also indicated is the horizontal liquid velocity $V_x(z)$ on the vapour pocket wall, from which the average wave velocity V_{wave} is determined, together with the vertical positions z_{crest} and z_{runup} of the wave crest and the run-up point, respectively.

Firstly, we determine the time evolution of the area $S(t)$ of the vapour pocket, starting from the impact moment at $t = t_{\text{impact}}$. From this quantity, the effective radius $R_{\text{eff}}(t)$ is determined by assuming that the cavity can be approximated as hemicylindrical, i.e. $S(t) = (1/2)\pi(R_{\text{eff}}(t))^2$ or $R_{\text{eff}}(t) = \sqrt{2S(t)/\pi}$. Next to the effective radius, we also determine the compressional velocity V_0 from the time rate of change of the surface area. This is done by identifying $V_0 = -(d/dt)R_{\text{eff}}(0)$, or, by differentiating $S(t) = (1/2)\pi(R_{\text{eff}}(t))^2$ as

$$\left. \frac{dS}{dt} \right|_{t=0} = \pi R_{\text{eff},0} \left. \frac{dR_{\text{eff}}}{dt} \right|_{t=0} \Rightarrow V_0 = -\frac{1}{\pi R_{\text{eff},0}} \left. \frac{dS}{dt} \right|_{t=0} = -\frac{1}{\sqrt{2\pi S(0)}} \left. \frac{dS}{dt} \right|_{t=0}, \quad (\text{B1})$$

where $R_{\text{eff},0} \equiv R_{\text{eff}}(0)$ and the minus sign has been inserted to make V_0 a positive quantity.

The second quantity that we determine from the images is the wetted length $\ell(t)$. This quantity is defined as the length of the liquid free surface that is in contact with the vapour

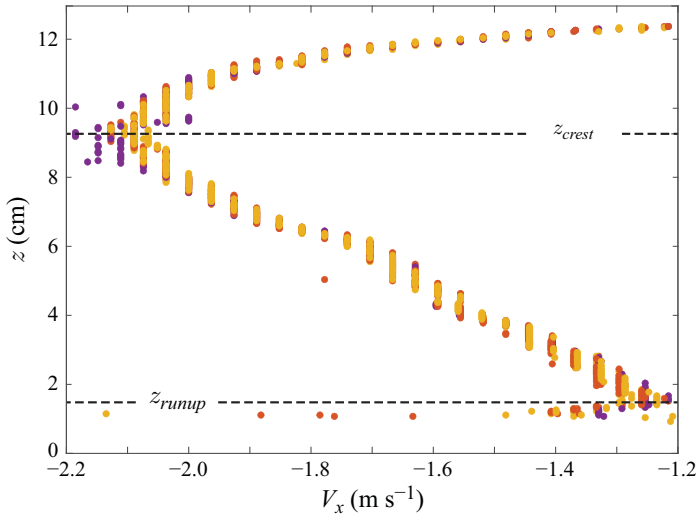


Figure 17. Horizontal velocity component V_x along the shape of five repetitions (different colours) of a wave with $\alpha = 0.385$ and $T_0 = 40\text{ }^\circ\text{C}$, as a function of the vertical coordinate z . The two dashed horizontal lines indicate the top (wave crest, at position z_{crest}) and the bottom (run-up point, at position z_{runup}) of the breaking wave just before impact. These are the positions between which the average V_{wave} has been calculated.

pocket in the cross-section. Clearly, since $\ell(t)W$ is the area over which the heat that is produced during condensation can be transported into the liquid, this is an important quantity to know – especially at the moment of impact, where we define $\ell_0 \equiv \ell(0)$.

The final quantity that we extract from the images is the horizontal velocity $V_x(z)$ along the cavity interface. This quantity is responsible for pressurising the region entrapped by the vapour pocket as expressed by $\Delta p = \rho_L V_{wave}^2$, which is derived from the pressure exerted by a jet hitting a surface. In figure 17 we show $V_x(z)$ for five repetitions of an experiment at $T_0 = 40\text{ }^\circ\text{C}$ with a wave shape of steepness $\alpha = 0.385$. We find that the data largely overlaps for the different repetitions, and that there is a clear, almost linear decrease of the magnitude of the velocity as one goes from the position z_{crest} where the crest of the wave impacts (upper horizontal dashed line) to the position z_{runup} of the bottom of the vapour pocket, where the liquid tends to rise (run up) due to conservation of mass. This is expected for a breaking wave, as the wave crest is in the process of overtaking the lower part of the wave. To determine an average wave speed V_{wave} , we average the data over the vertical coordinate

$$V_{wave} = -\frac{1}{z_{crest} - z_{runup}} \int_{z_{runup}}^{z_{crest}} V_x(z) dz, \tag{B2}$$

where, again, the minus sign is inserted to make V_{wave} a positive quantity.

Now, one may ask which pressure scale to take. Even if V_{wave} is much smaller than the speed of sound in water, it is known that the latter could reduce considerably in the presence of vapour bubbles, when it could become as small as approximately 10 m s^{-1} . However, due to the preparation of our experiments and the waiting time between them (15 mins), we are confident that there will be no vapour bubbles left in the flume at the moment that we start a new wave impact experiment. Therefore, compressibility effects are negligible at the impact speeds used in our experiments and the inertial pressure scale $\rho_L V_{wave}^2$ is the appropriate one to take.

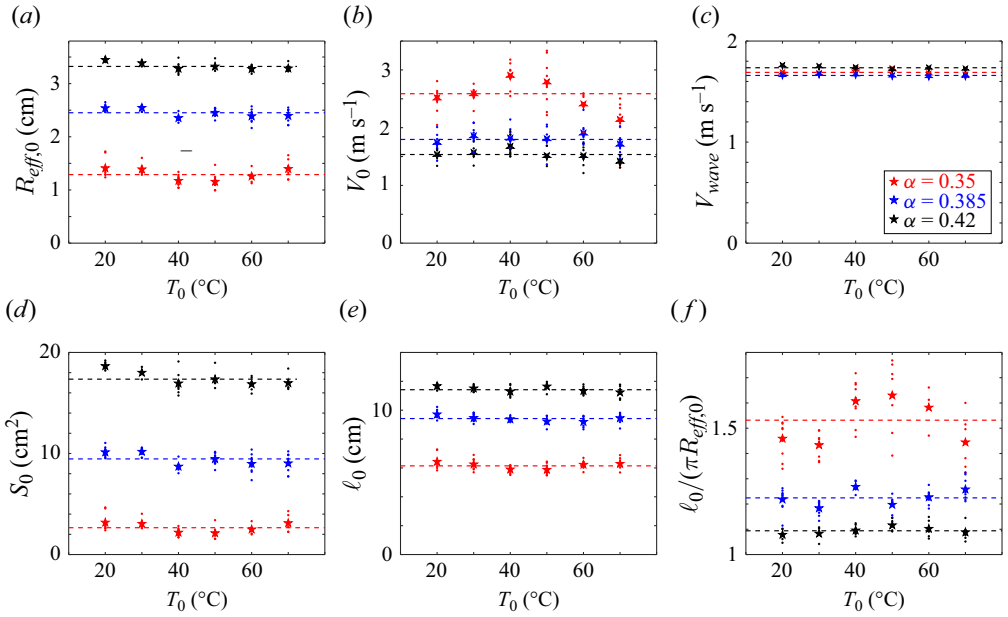


Figure 18. Wave shape parameters measured from the side view images of the waves, for all analysable experiments, as a function of temperature T_0 (horizontal axes) and wave steepness α (colours, see legend). (a) Effective vapour pocket radius $R_{eff,0}$ upon impact. (b) Compressional velocity V_0 of the vapour pocket upon impact. (c) Wave velocity V_{wave} . (d) Surface area S_0 of the vapour pocket upon impact. (e) Wetted length ℓ_0 of the vapour pocket upon impact. (f) Multiplication factor $\ell_0/(\pi R_{eff,0})$ upon impact.

α	$R_{eff,0}$ (cm)	S_0 (cm ²)	V_0 (m s ⁻¹)	V_{wave} (m s ⁻¹)	ℓ_0 (cm)	$\ell_0/(\pi R_{eff,0})$
0.35	1.29	2.65	2.59	1.69	6.14	1.53
0.385	2.45	9.46	1.80	1.66	9.42	1.22
0.42	3.32	17.4	1.54	1.74	11.4	1.09

Table 2. Temperature-averaged wave shape parameters for the different values of the wave steepness α . Here, S_0 is the cross-sectional vapour pocket area, $R_{eff,0}$ the effective radius, ℓ_0 the wetted length, V_0 the compressional velocity, V_{wave} the wave speed and $\ell_0/(\pi R_{eff,0})$ a multiplication factor representing the ratio of the wetted length to that of a hemicylindrical cavity of the same area.

In [figure 18](#) we report the above quantities for all cases where the analysis provides unambiguous results, as a function of both α and T_0 . In [figure 18\(a\)](#) the effective radius $R_{eff,0}$ upon impact is plotted versus T_0 for the three different α . Here, the dots represent values measured for individual experimental runs, whereas the star-shaped symbols indicate the average for each (T_0, α) pair. The horizontal dashed lines in turn show the temperature-averaged values, which are also reported in [table 2](#). Similar to other quantities reported, we find little spreading of the data with respect to different repetitions and with respect to average quantities. Moreover, the average values of $R_{eff,0}$ are nearly constant and, thus, appear to be independent of T_0 , which suggests that $R_{eff,0}$ is predominantly dependent on α . In contrast, $R_{eff,0}$ monotonically increases with α for all T_0 . The same can be said for the cross-sectional area S_0 of the vapour pocket, which is trivially related to $R_{eff,0}$, but reported for completeness in [figure 18\(d\)](#).

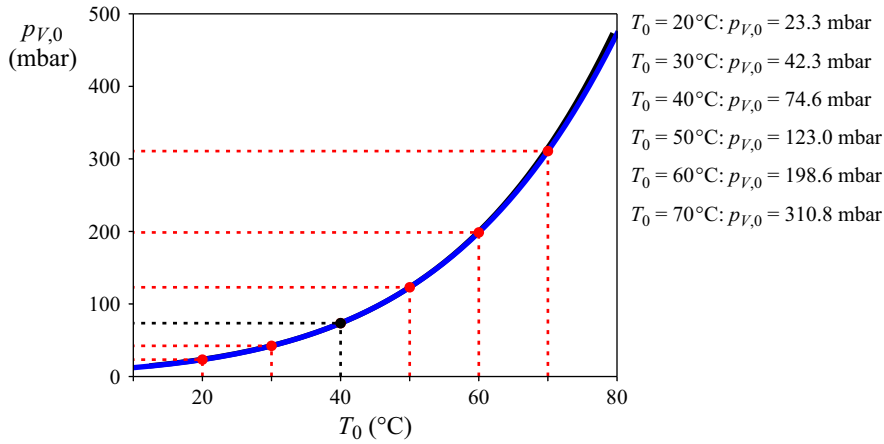


Figure 19. Vapour curve of water, representing the vapour pressure $p_{V,0}$ as a function of temperature T_0 (blue curve). Also indicated are the temperature set points used in this study (vertical dotted lines) and the corresponding vapour pressures (horizontal dotted lines), which are also tabulated next to the plot. Finally, the black curve largely hiding behind the vapour curve is the expression (C2) computed using $(T_0, p_{V,0}) = (40.0 \text{ }^\circ\text{C}, 74.6 \text{ mbar})$.

In figure 18(b) we plot the compressional velocity $\dot{R}(0) = -V_0$. In contrast to the effective radius, V_0 becomes larger for decreasing α , and also appears to be less constant as a function of temperature. Especially for $\alpha = 0.35$, the magnitude of the velocity becomes significantly larger than average for intermediate values of T_0 and subsequently decreases with increasing T_0 – however, we note that the spread in the data for a given T_0 is rather large. We note that when a small and slender cavity is formed, it is challenging to obtain a reliable tracing of the wave shape. As a consequence, this will yield errors in determining the boundary and, consequently, in $S(t)$. As V_0 explicitly depends on both S and \dot{S} (see (B1)), we expect large errors when the cavities are small, as is the case for $\alpha = 0.35$. This, we believe is the main source of the data spread in figure 18(b) for $T_0 > 40 \text{ }^\circ\text{C}$ and for $\alpha = 0.35$.

Figure 18(c) contains the wave speed V_{wave} , where the data has been obtained in a slightly different way, namely by taking all data for a certain (T_0, α) pair, removing outliers and subsequently determining the average over height z consistent with (B2). A very different picture emerges, where there is hardly any variation of V_{wave} , neither in α nor in T_0 and $V_{wave} \approx 1.7 \text{ m s}^{-1}$ throughout, where very small differences can be discerned in the second decimal.

Finally, figure 18(e) contains the wetted length $\ell_0 = \ell(0)$ at the moment of impact and figure 18(f) reports the multiplication factor $\ell_0/(\pi R_{eff,0})$, which represents the ratio of the wetted length to that of a hemicylindrical cavity of the same area. In this case, we find a larger degree of variability as compared with the other reported quantities. This is presumably due to this quantity being the result of two measured quantities. We note that the detected boundary of the vapour pocket (through edge detection) is smoothed using a polynomial fit of ninth order to obtain ℓ_0 . The temperature-averaged quantities represented by the horizontal dashed lines are summarised in table 2.

Appendix C. Thermodynamic state variables on the vapour curve

In figure 19 we plot the vapour curve of water using the Antoine equation with coefficients provided by the NIST Chemistry WebBook. Also indicated are the temperature set

points used in this study (vertical dotted lines) and the corresponding vapour pressures (horizontal dotted lines), which for reference, are also provided in numerical form to the right of the plot. In our experiments the vapour pressure ranges from 23.3 mbar (at 20 °C) to 310.8 mbar (at 70 °C). Note that a closed system that contains both a liquid and its vapour in contact through phase change will move towards a thermal equilibrium state where the temperature of the system and the (partial) pressure of the vapour lie on the vapour curve.

For a vapour described by the ideal gas law, the Clausius-Clapeyron equation, which locally describes the vapour curve far away from the critical point, states that

$$\frac{dp_V}{dT_V} = \frac{Lp_V}{\mathcal{R}_s T_V^2}, \tag{C1}$$

with L the latent heat of vaporisation and \mathcal{R}_s the specific gas constant of the vapour. Starting from an equilibrium point $p_{V,0}, T_0$ on the vapour curve this equation can be directly integrated using separation of variables as

$$\frac{T_V(p_V)}{T_0} = \left[1 - \beta \log \left(\frac{p_V}{p_{V,0}} \right) \right]^{-1} \tag{C2}$$

where $\beta \equiv \mathcal{R}_s T_0 / L$. Using the ideal gas law, $p_V = \rho_V \mathcal{R}_s T_V$, one may subsequently express ρ_V in terms of p_V :

$$\frac{\rho_V(p_V)}{\rho_{V,0}} = \frac{p_V}{p_{V,0}} \left[1 - \beta \log \left(\frac{p_V}{p_{V,0}} \right) \right]. \tag{C3}$$

Here $\rho_{V,0} = p_{V,0} / (\mathcal{R}_s T_0)$ is the vapour density at the equilibrium point $p_{V,0}, T_0$. For small changes $\delta p_V = p_V - p_{V,0}$, $\delta T_V = T_V - T_0$ and $\delta \rho_V = \rho_V - \rho_{V,0}$ from the equilibrium point, one may linearise the above expressions to give

$$\frac{\delta \rho_V}{\rho_{V,0}} \approx \frac{\delta p_V}{p_{V,0}} \quad \text{and} \quad \frac{\delta T_V}{T_0} \approx \beta \frac{\delta p_V}{p_{V,0}}, \tag{C4}$$

that is, relative changes in density and pressure are similar, whereas relative changes in temperature are smaller by a factor β . Also useful may be the following expression for the derivative of the density with respect to the pressure:

$$\frac{\partial \rho_V}{\partial p_V} = \frac{\rho_V}{p_V} - \frac{1}{L}. \tag{C5}$$

Expression (C2) gives a very accurate expression of the vapour curve in a sizeable neighbourhood of a starting point $(T_0, p_{V,0})$ on the vapour curve. As an example, we take $(T_0, p_{V,0}) = (40.0 \text{ °C}, 74.6 \text{ mbar})$ in figure 19 and use (C2) to compute the temperature as a function of the vapour pressure, leading to the black curve in the plot, that is for largest part coinciding with the vapour curve.

Appendix D. The boundary condition at the impact wall

In the main text we adopted an adiabatic boundary condition at the impact wall for our vapour pocket dynamics model (cf. § 4 and figure 9). In this Appendix we discuss this boundary condition in more detail. In general, one may distinguish two quite different situations.

(i) Prior to impact the wall is dry: in this case there is no two-phase contact at or near the wall and no condensation can take place. The vapour can be locally supercooled in

this case (until reaching the spinodal curve where spontaneous phase separation will take place), which also remains true if the temperature of the wall is lower than the ambient temperature T_0 . In the dry wall case, there may however be a parasitic heat flux q''_{par} in the vapour, from the liquid–vapour interface to the wall, which, for simplicity, we take to be a perfectly conducting heat sink at the ambient temperature T_0 . The latter approximation stands to reason, since the heat conductivity of steel is at least an order of magnitude larger than that of the water, and also constitutes the worst case scenario where the wall is perfectly conducting. Now we may estimate the magnitude of the parasitic heat flux as $q''_{par} \sim k_V \Delta T/R$, where k_V is the heat conductivity of the vapour and we used the fact that the typical size of the bubble should scale as the bubble radius R . For the regular heat flux into the liquid, we may estimate $q''_{reg} \sim k_L \Delta T/\sqrt{\pi\alpha_L t}$, which is a lower estimate for the heat flux into the liquid (since, in general, the temperature inside the vapour bubble is not constant but will go up during the impact, which will partly erase the thermal boundary layer in the liquid as it is being formed). The ratio between parasitic and regular heat flux now becomes

$$\frac{q''_{par}}{q''_{reg}} \sim \frac{k_V}{k_L} \frac{\sqrt{\pi\alpha_L t}}{R} \approx 1 \times 10^{-4} \ll 1 \tag{D1}$$

where we estimated $k_V \approx 0.016 \text{ W m}^{-1}\text{K}^{-1}$, $k_L \approx 0.6 \text{ W m}^{-1}\text{K}^{-1}$, $\alpha_L \approx 1.5 \times 10^{-7} \text{ m}^2\text{s}^{-1}$, $R \approx 2 \text{ cm}$ and $t = t_{i,0} \approx 10 \text{ ms}$ as the typical duration of the (first) compression phase (cf. Figure 10) to arrive at the numerical estimate. Note that the use of a quasi-steady approximation for the heat flux in the vapour phase can be motivated from the observation that the heat diffusivity in the vapour phase is typically one to two orders of magnitude larger than that in the liquid phase: $\alpha_V \gg \alpha_L$. Clearly, the parasitic heat flux through the vapour bubble is negligible compared with the heat flux into the liquid and the wall can be assumed to be adiabatic in this case.

(ii) Prior to impact the wall is wetted: in this second case, we may assume that a liquid film is present on the wall and has a micrometric thickness h_0 . Now, condensation can in principle occur at the wall, and there will be an initial time t_i at which the condensation heat will penetrate the liquid film until it reaches the wall, which can be estimated by equating the thermal boundary layer thickness $\delta_{th} \approx \sqrt{\pi\alpha_L t}$ with h_0 :

$$t_i \approx \frac{h_0^2}{\pi\alpha_L} \tag{D2}$$

Now, in the situation that t_i is longer than the duration of the first compression phase in our experiment, δ_{th} remains smaller than the film thickness and the surface area of our hemicylindrical bubble in the energy-mass balance equation (4.1) is simply extended by the contact area of the bubble and the liquid film, i.e. one needs to substitute $\pi RW \rightarrow (\pi + 2)RW$ in the last term on the right-hand side of (4.2), leading to a multiplicative factor $(2R(t) + \pi R(t))/(\pi R(t)) \approx 1.64$ before that term. As stated above, the typical duration of the first compression phase is smaller than $t_{i,0} = 10 \text{ ms}$, such that the above condition will be met for film thicknesses larger than $h_{0,min} \sim \sqrt{\pi\alpha_L t_{i,0}} \approx 70 \text{ }\mu\text{m}$.

What is the situation that is most likely to occur in our experiments? Although this is a hard question to answer since we have no direct evidence of the presence of a water film on the impact wall, we may have a look at the possible options. If the wall would be dry (e.g. because its temperature turns out to be slightly higher than the environment), the boundary condition taken in the model would be correct and no modifications would be necessary. This is definitely the case that is expected to occur during cryogenic liquid transport, since

due to the fact that the surroundings are at a much higher temperature, walls are expected to be slightly hotter than the liquid, preventing the formation of a liquid film on the walls.

If a liquid film is deposited on the impact wall, then it will be done so by the liquid moving down along the impact wall, just prior to the impact, where it needs to be noted that the vapour pocket dynamics (collapse) is occurring below the quiescent water level in the flume. Since this then will happen with a velocity of the order of the impact speed, we may estimate the film thickness using the Landau–Levich–Derjaguin (LLD) equation $h_0 = \sqrt{\sigma/(\rho_L g)} Ca^{2/3}$ with $Ca = \mu_L U_r / \sigma$, with $\mu_L \approx 1.0$ mPa s the dynamic viscosity of water, which for a (small) rise speed of $U_r = 0.73$ m/s, equals $Ca = 0.01$, which is also on the upper validity boundary of the LLD equation. Inserting $Ca = 0.01$ we find a lower limit $h_0 \approx 120 \mu\text{m}$, which is larger than $h_{0,min}$. Therefore, taking the presence of a liquid film into account, we have to multiply the second term on the right-hand side of (4.2) with a factor of 1.64, which needs to be done in all subsequent steps leading to a redefinition of Π multiplying with the same multiplicative factor 1.64. This will lead to a slight but equal right shift of all data points in figure 12, which will leave our conclusions unaltered.

Appendix E. An axisymmetric version of the Plesset-Zwick relation

Following the same procedure outlined in Plesset & Zwick 1952, where a solution to the spherically symmetric convective heat equation was derived in the limit of a thin thermal boundary layer, we start from the axisymmetric, convective heat equation

$$\frac{\partial \Delta T}{\partial t} + u_r \frac{\partial \Delta T}{\partial r} = \frac{\alpha_L}{r} \frac{\partial}{\partial r} \left(r \frac{\partial \Delta T}{\partial r} \right), \tag{E1}$$

with $\Delta T = T(r, t) - T_0$, and where, for an incompressible liquid, the radial velocity component can be written as $u_r = R\dot{R}/r$. Now, if we transform r and t to the so-called Lagrangian coordinates $h(r, t) = (1/2)(r^2 - R(t)^2)$ and t , we transform (E1) into

$$\frac{\partial \Delta T}{\partial t} = \alpha_L \frac{\partial}{\partial h} \left(r^2 \frac{\partial \Delta T}{\partial h} \right) = \alpha_L \frac{\partial}{\partial h} \left([2h + R(\tau)^2] \frac{\partial \Delta T}{\partial h} \right), \tag{E2}$$

where ΔT now needs to be read as a function of h and t , i.e. $\Delta T(h, t) = \Delta T(r(h, t), t)$. The next step is to define a quantity U with $\Delta T = \partial U / \partial h$, or

$$U(h, t) = - \int_{h'=h}^{\infty} \Delta T(h', t) dh'. \tag{E3}$$

If we now take the derivative of U with respect to t and make use of (E2), we obtain

$$\frac{\partial U}{\partial t} = - \int_{h'=h}^{\infty} \frac{\partial \Delta T(h', t)}{\partial t} dh' = \alpha_L [2h + R(t)^2] \frac{\partial \Delta T}{\partial h} = \alpha_L [2h + R(t)^2] \frac{\partial^2 U}{\partial h^2}, \tag{E4}$$

and defining a new time variable κ with $\partial \kappa / \partial t = R(t)^2$ as

$$\kappa = \int_{t'=0}^t R(t')^2 dt' \tag{E5}$$

we obtain, using $\partial U / \partial \kappa = (\partial U / \partial t) / (\partial \kappa / \partial t) = (\partial U / \partial t) / R(t)^2$ from (E4),

$$\frac{\partial U}{\partial \kappa} = \alpha_L \left[1 + \frac{2h}{R(\tau)^2} \right] \frac{\partial^2 U}{\partial h^2}. \tag{E6}$$

At this point we invoke the assumption that the boundary layer is thin, namely, $\delta \ll R$, with δ the boundary layer thickness. Now the only place where $\Delta T = \partial U / \partial h$ is non-zero is in

the boundary layer, i.e. in $R \leq r \leq R + \delta$. Squaring this inequality we find that $R^2 \leq r^2 \leq (R + \delta)^2$, or subtracting R^2 , that $0 \leq r^2 - R^2 \leq 2R\delta + \delta^2$. Noting that the middle quantity is equal to $2h$ and dividing by R^2 , we obtain

$$0 \leq \frac{2h}{R^2} \leq 2\frac{\delta}{R} + \frac{\delta^2}{R^2} \ll 1, \tag{E7}$$

where the last inequality follows from the thinness of the boundary layer. We thus find that $2h/R^2 \ll 1$ and, consequently, in the thin boundary layer limit (E6) reduces to the one-dimensional, purely diffusive heat equation

$$\frac{\partial U}{\partial \kappa} = \alpha_L \frac{\partial^2 U}{\partial h^2}. \tag{E8}$$

This equation must be supplemented by an initial condition and two boundary conditions. The initial condition follows directly from $\Delta T(r, t = 0) = 0$ for all $r \geq R$, which directly leads to $\partial U/\partial h(h, \kappa = 0) = 0$ for all $h \geq 0$ (since $\kappa = 0$ corresponds to $t = 0$). From this we find that $U(h, \kappa = 0)$ must be constant. Since the physics lies in the derivative of U , we may, however, without loss of generality, take this constant to be zero, leading to $U(h, \kappa = 0) = 0$.

The boundary condition at infinity follows from $\lim_{r \rightarrow \infty} \Delta T(r, t) = 0$, which leads directly to $\lim_{h \rightarrow \infty} U(h, \kappa) = 0$. For the last boundary condition, we realise that we want to relate the (known) temperature inside the bubble $\Delta T(R(t), t) \equiv f(t)$ to the (unknown) temperature gradient at the bubble wall inside the liquid, $[\partial \Delta T/\partial r](R(t), t) \equiv g(t)$, which are both functions of time t only. Translated to $U(h, \kappa)$ this becomes

$$\left. \frac{\partial U}{\partial h} \right|_{h=0} = f(\kappa) \quad \text{and} \quad \left. \frac{\partial^2 U}{\partial h^2} \right|_{h=0} = \frac{g(\kappa)}{R(\kappa)} \equiv J(\kappa), \tag{E9}$$

where $f(\kappa) = f(t(\kappa))$, etc. Now, to solve (E8), we perform a Laplace transformation $\mathcal{L}[\]$ in the time variable κ , defined as

$$u(h, \lambda) \equiv \mathcal{L}[U(h, \kappa)] \equiv \int_{\kappa=0}^{\infty} e^{-\kappa\lambda} U(h, \kappa) d\kappa. \tag{E10}$$

The Laplace transform of (E8) leads to

$$\lambda u(h, \lambda) - U(h, \kappa=0) = \alpha_L \frac{\partial^2 u}{\partial h^2}, \tag{E11}$$

which with the initial condition $U(h, \kappa=0) = 0$ leads to the general solution

$$u(h, \lambda) = A \exp\left(-\sqrt{\frac{\lambda}{\alpha_L}} h\right) + B \exp\left(+\sqrt{\frac{\lambda}{\alpha_L}} h\right), \tag{E12}$$

with A, B unknown integration constants. The Laplace transformed boundary condition at infinity ($\lim_{h \rightarrow \infty} u(h, \lambda) = 0$) leads to the conclusion that $B = 0$, whereas A follows from the Laplace transform of the second condition in (E9). Defining $\mathcal{L}[J(\kappa)] \equiv j(\lambda)$ we thus find that

$$\left. \frac{\partial^2 u}{\partial h^2} \right|_{h=0} = j(\lambda) \quad \Rightarrow \quad A = j(\lambda) \frac{\alpha_L}{\lambda} \quad \Rightarrow \quad u(h, \lambda) = j(\lambda) \frac{\alpha_L}{\lambda} \exp\left(-\sqrt{\frac{\lambda}{\alpha_L}} h\right), \tag{E13}$$

with which we have found the solution of our boundary value problem in Laplace space. Computing the quantity of interest $\partial u/\partial h$ at $h = 0$ we obtain

$$\frac{\partial u}{\partial h} \Big|_{h=0} = -j(\lambda) \sqrt{\frac{\alpha_L}{\lambda}}, \tag{E14}$$

which can be formally transformed back to the κ domain as

$$\frac{\partial U}{\partial h} \Big|_{h=0} = \mathcal{L}^{-1} \left[\frac{\partial u}{\partial h} \Big|_{h=0} \right] = -\mathcal{L}^{-1} [j(\lambda)] \otimes \mathcal{L}^{-1} \left[\sqrt{\frac{\alpha_L}{\lambda}} \right], \tag{E15}$$

where $\mathcal{L}^{-1}[\]$ represents the inverse Laplace transform and \otimes denotes a convolution of the two functions. The first inverse is just $J(\kappa)$ and the second one can be found in any Laplace transform table to give $\sqrt{\alpha_L/(\pi\kappa)}$ such that

$$\frac{\partial U}{\partial h} \Big|_{h=0} = -J(\kappa) \otimes \sqrt{\frac{\alpha_L}{\pi\kappa}} = -\sqrt{\frac{\alpha_L}{\pi}} \int_{\xi=0}^{\kappa} \frac{J(\kappa)}{\sqrt{\kappa-\xi}} d\xi, \tag{E16}$$

Now, using the definition of κ in (E5) and calling the time integration variable s , i.e. $\xi = \int_{w=0}^s R(w)^2 dw$, we find that $d\xi = R(s)^2 ds$ and

$$\sqrt{\kappa-\xi} = \sqrt{\int_{w=0}^t R(w)^2 dw - \int_{w=0}^s R(w)^2 dw} = \sqrt{\int_{w=s}^t R(w)^2 dw}, \tag{E17}$$

with which (E15), remembering from the definition of U in (E3) that $[\partial U/\partial h]_{h=0} = \Delta T(r=R, t) = T_V - T_0$ and that $J(\kappa) = g(\kappa)/R(\kappa) = (1/R)(\partial \Delta T/\partial r)_{r=R}$ as defined earlier (E9), directly leads to the axisymmetric version of the Plesset–Zwick formula

$$T_V - T_0 = -\sqrt{\frac{\alpha_L}{\pi}} \int_{s=0}^t \frac{R(s) \frac{\partial T}{\partial r} \Big|_{r=R(s)}}{\sqrt{\int_{w=s}^t R(w)^2 dw}} ds. \tag{E18}$$

Appendix F. Average model pressure on the sensor area

When we want to connect the measured pressures with the pressures predicted by the model, we need to take into account that as long as the sensor is completely covered by the bubble it will measure the vapour pressure $p_V(t)$ in the bubble, but as soon as it becomes smaller than the sensor radius, the sensor signal is partly caused by the pressure in the vapour bubble and partly by the pressure of the surrounding liquid. To analyse this, we start from the idealised situation where the vapour bubble and the sensor share the same horizontal symmetry axis (as sketched in figure 9b) and where the sensor area is assumed to be square instead of circular, as sketched in the inset of figure 11(d).

Let us start by computing the pressure inside the liquid surrounding the bubble in the context of potential flow, including surface tension. The flow field in the liquid can be computed from the continuity equation giving $v_r(r, t) = R\dot{R}/r$. The defining equation for the flow potential, $v_r = \partial\varphi/\partial r$, can be directly integrated to

$$\varphi(r, t) = R\dot{R} \log[r/R_{sensor}] + f(t) \quad \Rightarrow \quad \frac{\partial\varphi}{\partial t} = \frac{d}{dt}(R\dot{R}) \log[r/R_{sensor}] + \dot{f} \tag{F1}$$

where f is an arbitrary function of time. Using the unsteady Bernoulli equation from a point $r = R^+$ just outside the bubble, where $p_L(R^+, t) = p_V(t) - \sigma/R$, to a point r we obtain

$$p_L(R^+, t) + \frac{1}{2}\rho_L v(R^+, t)^2 + \rho_L \left. \frac{\partial \varphi}{\partial t} \right|_{r=R^+} = p_L(r, t) + \frac{1}{2}\rho_L v(r, t)^2 + \rho_L \left. \frac{\partial \varphi}{\partial t} \right|_{r=r} \tag{F2}$$

Using the above expressions for v_r and $\partial \varphi / \partial t$, we thus find an expression for $p_L(r, t)$,

$$p_L(r, t) = p_V(t) - \frac{\sigma}{R} + \frac{1}{2}\rho_L \dot{R}^2 \left(1 - \frac{R^2}{r^2} \right) + \rho_L \frac{d}{dt}(R\dot{R}) \log[R/r] \tag{F3}$$

with which

$$p(r, t) = \begin{cases} p_V(t) & \text{if } r \leq R, \\ p_L(r, t) & \text{if } r > R. \end{cases} \tag{F4}$$

To determine the average pressure on the sensor, we need to integrate the above pressure $p(r, t)$ over the sensor surface and divide by the latter. Using the abbreviation $R_s \equiv R_{sensor}$ for convenience,

$$p_{sensor}(t) = \frac{1}{R_s} \int_{r=0}^{R_s} p(r, t) dr = \frac{1}{R_s} \left[p_V(t)R + \int_{r=R}^{R_s} p_L(r, t) dr \right] \tag{F5}$$

where it is understood that this expression holds only for $R < R_{sensor}$ as for $R \geq R_{sensor}$, we have $p_{sensor}(t) = p_V(t)$. It is now straightforward, albeit a bit tedious, to carry out the integration, which ultimately leads to

$$p_{sensor}(t) = p_V(t) - \frac{\sigma}{R} \left[1 - \frac{R}{R_s} \right] + \frac{1}{2}\rho_L \dot{R}^2 \left[1 - \frac{R}{R_s} \right]^2 + \rho_L \frac{d}{dt}(R\dot{R}) \left[1 - \frac{R}{R_s} - \log \frac{R_s}{R} \right]. \tag{F6}$$

To calculate $p_{sensor}(t)$ using the numerical solution from (4.2), (4.3) and (4.5) with initial value conditions (4.6), it is practical to eliminate the acceleration term $d(R\dot{R})/dt$ using the Rayleigh–Plesset equation (4.3). Also note that, for completeness, we have included the surface tension term, both in this appendix and in the numerical calculations reported in this paper, but it can of course be neglected, given the large value of the Weber number.

Appendix G. Comparison of results from the phase-change model of § 4 with a non-condensable gas model

Since an adiabatic compression model would also predict an increase of the pressure in the vapour pocket at lower ambient vapour pressures, one of the questions raised in the main text was how much of the observed high pressures in the model at lower temperatures are due to condensation and how much is just due to the fact that the equilibrium vapour pressure rapidly decreases with temperature. In this appendix we directly compare the results obtained from our model for the vapour pocket dynamics (figures 10 and 11), with those obtained from the numerical solution of the two-dimensional Rayleigh–Plesset equation (4.3), supplemented with an adiabatic model for the ‘vapour’ in the pocket, namely

$$p_V(t) = p_{V,0} \frac{V_0^\gamma}{V(t)^\gamma} = \frac{p_{V,0} R_0^{2\gamma}}{R(t)^{2\gamma}} \tag{G1}$$

where $V(t)$, V_0 are the volume of the pocket at time t and $t = 0$, respectively, and γ is the adiabatic constant (specific heat ratio) for water vapour. This implies that we are solving the adiabatic model from exactly the same initial conditions as the vapour pocket dynamics model, but without including phase change, such that the ‘vapour’ would behave as a non-condensable gas with exactly the same properties as water vapour.

The results of this calculation are found in [figure 20](#). We first turn to the time evolution of the radius $R(t)$, where [figure 20\(b\)](#) contains the same data as (a) but zoomed in to the first 10 ms, highlighting the first compression of the pocket. From the latter plot, it appears that the adiabatic-model curves for all temperatures initially follow the same path as those of the phase-change one, but subsequently compress less, with $R(t)$ larger than in the phase-change case. This stands to reason since condensation will decrease the vapour content inside the vapour pocket, making it easier to compress than in the adiabatic case. This is consistent with the corresponding time evolution of the pressure plotted in [figure 20\(d\)](#), where we indeed find that, at least initially, the pressure for the adiabatic case is larger than that for the phase-change case.

Another difference that is clearly visible in [figure 20\(b\)](#) is that the minimum radius attained for the phase-change model is much smaller than that reached in the adiabatic model: in the latter case, the radius never becomes smaller than the sensor radius indicated by the horizontal dotted black line, whereas for the phase-change model the radius can become very small, especially for the lowest two temperatures due to an almost complete condensation of the vapour contents of the pocket. This reflects in the behaviour of the pressure ([figure 20d](#)), where it is seen that the pressure in the phase-change model shoots up to very large values for the lowest two temperatures (20 °C and 40 °C), much surpassing the maximum values observed in the adiabatic case, whereas the behaviour for the largest two temperatures (60 °C and 80 °C) is opposite: here the maximum values for the phase-change case remain smaller than those of the adiabatic case. This last observation is connected to the value of the parameter Π (see 4.14): if Π is larger than 1, the condensation rate is strong enough to overpower compression of the vapour contents inside the pocket, and essentially provoking a Rayleigh collapse of the pocket, whereas when $\Pi < 1$, this is not the case and sufficient vapour is remaining to create oscillatory behaviour of the vapour pocket.

Turning to the longer time series ([figures 20a,c](#)), the main difference that catches the eye is that the adiabatic oscillations are undamped. The reason is clear, since – with the exclusion of the viscous term in the Rayleigh–Plesset equation – no dissipation is present in the system. In reverse, this implies that the strong damping observed in the phase-change model is solely due to phase change, where successive condensation and evaporation half-cycles, concurring with storage and retraction of energy in the thermal boundary layer in the liquid that surrounds the pocket, are responsible for the observed damping. Therefore, also at higher temperatures, phase change may not be the overwhelmingly dominant factor, but its influence on the dynamics remains non-negligible. In addition, there is also a pronounced increase of the period of the oscillations, as would be expected for a strongly damped signal.

The last plot, [figure 20\(e\)](#), shows the comparison of the pressure-sensor-integrated values for the maximum pressure $P_{sensor,max}$ for the two models on a logarithmic scale, as a function of ambient temperature T_0 . For high temperatures, $P_{sensor,max}$ is observed to be slightly larger for the adiabatic model (red symbols) than for the phase-change model (blue symbols). This however rapidly changes around the temperature for which $\Pi \approx 1$, where the pressure in the phase-change case changes steeply, whereas the pressure in the adiabatic case continues to change gradually. In the low-temperature regime where the very large pressures are observed, the pressure predicted by the phase-change model is almost

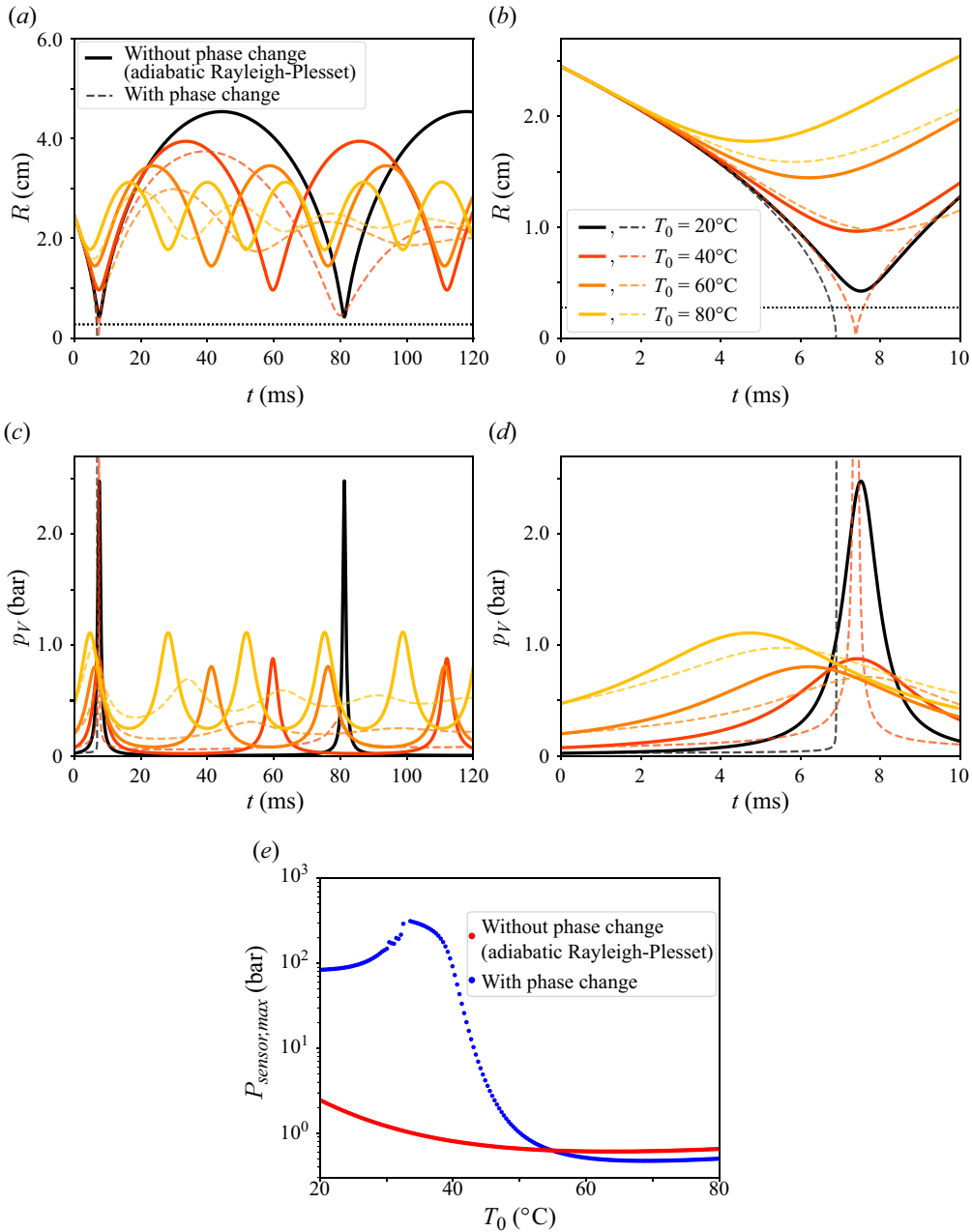


Figure 20. (a) Solution of the adiabatic model (solid curves) compared with that of the phase-change model from § 4 (dashed lines, also plotted in figures 10 and 11) using the parameters observed for a wave of steepness $\alpha = 0.385$ in both cases. (a) The vapour bubble radius $R(t)$ as a function of time t for four different temperatures, $T = 20, 40, 60$ and 80 °C. The horizontal dashed line indicates the radius of the pressure sensors used, $R_{sensor} = 2.75$ mm. (b) Same data as in (a) but zoomed in on the region until the first minimum occurs. (c) The vapour pressure $p_V(t)$ as a function of time t . (d) Same data as in (c) but zoomed in on the region until the first minimum occurs. (e) Maximum pressure $P_{sensor,max}$, integrated over the sensor area, obtained using the phase-change model (blue symbols) and using the adiabatic model (red symbols), as a function of ambient temperature T_0 . Note that in the latter case no sensor integration was necessary since the pocket in all investigated cases remained larger than the sensor size. In plots (c,d) absolute pressures p are reported, whereas in (e) we use gauge pressures $P = p - p_{V,0}$, where $p_{V,0}$ is the equilibrium vapour pressure.

two orders of magnitude larger than that predicted by the adiabatic model. In conclusion, compared with the adiabatic model, the phase-change model predicts significant changes in the dynamics of the vapour pocket throughout the entire range of temperatures studied. The most significant aspect for the current work is that at low temperatures the pressure increase predicted by the adiabatic model is dwarfed by the enormous pressure rise predicted by the phase-change model.

Whoever may have been surprised that the pressure $P_{sensor,max}$ does not decrease monotonically with temperature (or with increasing vapour pressure), may be reassured by the fact that the rescaled pressure $P_{sensor,max}/p_{V,0} = (p_{sensor,max} - p_{V,0})/p_{V,0}$ does indeed decrease monotonically.

Appendix H. Full axisymmetric and spherically symmetric models

For completeness, we also provide the full axisymmetric model (4.2), (4.3) and (4.5) and initial conditions (4.6), including the surface tension and viscous terms (which only surface in the Rayleigh–Plesset equation), together with their non-dimensional form, analogous to (4.13), but including the non-dimensionalised form of the Plesset–Zwick equation. In addition, we provide the analogous equations for a completely spherical vapour bubble.

With the definitions introduced in §4.1, the full axisymmetric model, including surface tension σ and kinematic liquid viscosity ν_L can be written as

$$\frac{d}{dt}(R\dot{R}) \log\left[\frac{R_\infty}{R}\right] - \frac{1}{2}\dot{R}^2 + \frac{\sigma}{\rho_L R} + 2\nu_L \frac{\dot{R}}{R} + \frac{p_{V,0} - p_V(t)}{\rho_L} = 0, \quad (H1a)$$

$$\frac{dp_V}{dt} = \left(\frac{\partial \rho_V}{\partial p_V}\right)^{-1} \left[-\frac{2\rho_V}{R} \frac{dR}{dt} + \frac{2k_L}{LR} \frac{\partial T}{\partial r} \Big|_{r=R(t)} \right], \quad (H1b)$$

$$T_V - T_0 = -\sqrt{\frac{\alpha_L}{\pi}} \int_{s=0}^t \frac{R(s) \frac{\partial T}{\partial r} \Big|_{r=R(s)}}{\sqrt{\int_{w=s}^t R(w)^2 dw}} ds, \quad (H1c)$$

$$R(0) = R_0, \quad \dot{R}(0) = -V_0, \quad p_V(0) = p_{V,0} + \rho_L V_{wave}^2. \quad (H1d)$$

Using the same non-dimensionalisation procedure followed in §4.1, we obtain the dimensionless form of this set of equations:

$$\left(\frac{d}{d\tilde{t}}(\tilde{R}\dot{\tilde{R}})\right) \log\left[\frac{\tilde{R}_\infty}{\tilde{R}}\right] - \frac{1}{2}\dot{\tilde{R}}^2 + \frac{1}{We\tilde{R}} + 2\frac{\dot{\tilde{R}}}{Re\tilde{R}} - \tilde{\Delta} = 0, \quad (H2a)$$

$$\frac{d\tilde{\Delta}}{d\tilde{t}} = \frac{2}{Eu_0} \left(\frac{\partial \tilde{\rho}_V}{\partial \tilde{p}_V}\right)^{-1} \left[-\tilde{\rho}_V \frac{\dot{\tilde{R}}}{\tilde{R}} - \Pi \frac{\tilde{\Theta}}{\tilde{R}} \right], \quad (H2b)$$

$$\tilde{\Delta} = -\frac{1}{\pi} \int_{\tilde{s}=0}^{\tilde{t}} \frac{\tilde{R}(\tilde{s}) \tilde{\Theta}}{\sqrt{\int_{\tilde{w}=\tilde{s}}^{\tilde{t}} \tilde{R}(\tilde{w})^2 d\tilde{w}}} d\tilde{s}, \quad (H2c)$$

$$\tilde{R}(0) = 1; \quad \dot{\tilde{R}}(0) = -1; \quad \tilde{\Delta}(0) = \kappa. \quad (H2d)$$

Here, the dimensionless quantities $\tilde{\Delta}$, Π and κ are as defined in (4.11), (4.13c) and (4.14), whereas $We = \rho_L V_0^2 R_0/\sigma$ and $Re = V_0 R_0/\nu_L$ denote the Weber and Reynolds numbers, respectively. The Rayleigh–Plesset equation found in §4.3 corresponds to the

limit $We \rightarrow \infty$ and $Re \rightarrow \infty$. More importantly, we introduced a new dimensionless quantity $\tilde{\Theta}$ defined as

$$\tilde{\Theta} \equiv \frac{1}{\beta Eu_0 T_0} \sqrt{\frac{\pi \alpha_L R_0}{V_0}} \left. \frac{\partial T}{\partial r} \right|_{r=R}. \tag{H3}$$

Although it may not be immediately clear why this quantity should be of order one, it can be easily verified by inserting the approximation $(\partial T / \partial r)_{r=R} \approx (T_V - T_0) / \sqrt{\pi \alpha_L t}$ to obtain $\tilde{\Theta} \approx (\tilde{T}_V - 1) / (\beta Eu_0 \sqrt{\tilde{t}}) \approx \tilde{\Delta} / \sqrt{\tilde{t}}$, which is order one by construction, as argued in § 4.3. One may however arrive to this conclusion also from a more formal study of the properties of (H2c), noting that the function of the history factor $\tilde{R}(\tilde{s}) / \sqrt{\int_{\tilde{w}=\tilde{s}}^{\tilde{t}} \tilde{R}(\tilde{w})^2 d\tilde{w}}$ is to give a weight to $\tilde{\Theta}(\tilde{s})$ that rapidly decays to zero when the distance to \tilde{t} (i.e. $\tilde{t} - \tilde{s}$) becomes larger. Finally, one may ask if it is not necessary to provide an initial condition $\tilde{\Theta}(0)$. By expanding (H2c) around $\tilde{t} = 0$ for small $\tilde{t} = \tilde{\varepsilon}$ one can show that

$$\lim_{\tilde{\varepsilon} \rightarrow 0} \tilde{\Theta}(\tilde{\varepsilon}) = \lim_{\tilde{\varepsilon} \rightarrow 0} \frac{\pi \tilde{\Delta}(\tilde{\varepsilon})}{\sqrt{\tilde{\varepsilon}}}, \tag{H4}$$

which is all fine if $\tilde{\Delta}(\tilde{\varepsilon})$ goes to zero fast enough, in which case $\tilde{\Theta}(0) = 0$, but a bit problematic if $\tilde{\Delta}(0)$ is finite, as it is in the case of (H2d), since then $\tilde{\Theta}(0) = \infty$, which physically corresponds to the creation of a thermal boundary layer from an untouched liquid at a temperature T_0 lower than that at the boundary. A simple numerical workaround is to use $\tilde{\Theta}(0) = 0$ in all cases, where the small numerical error made close to $\tilde{t} = 0$ is rapidly corrected.

Finally, as in § 5, we discussed the extension of the applicability of the model to spherical vapour bubbles, we also present the spherically symmetric formulation, which follows from combining the spherically symmetric Rayleigh–Plesset equation (Brennen 2013) with the spherically symmetric version of the Plesset–Zwick formula from Plesset & Zwick 1952 and by inserting $m_V = (4/3)\pi R^3 \rho_V$ into our energy-mass balance (4.1), leading to

$$R\ddot{R} + \frac{3}{2}\dot{R}^2 + \frac{2\sigma}{\rho_L R} + 4\nu_L \frac{\dot{R}}{R} + \frac{p_{V,0} - p_V(t)}{\rho_L} = 0, \tag{H5a}$$

$$\frac{dp_V}{dt} = \left(\frac{\partial \rho_V}{\partial p_V} \right)^{-1} \left[-\frac{3\rho_V \dot{R}}{R} + \frac{3k_L}{LR} \left. \frac{\partial T}{\partial r} \right|_{r=R(t)} \right], \tag{H5b}$$

$$T_V - T_0 = -\sqrt{\frac{\alpha_L}{\pi}} \int_{s=0}^t \frac{R(s)^2 \left. \frac{\partial T}{\partial r} \right|_{r=R(s)}}{\sqrt{\int_{w=s}^t R(w)^4 dw}} ds, \tag{H5c}$$

$$R(0) = R_0, \quad \dot{R}(0) = -V_0, \quad p_V(0) = p_{V,0} + \rho_L V_{wave}^2, \tag{H5d}$$

which then leads to the dimensionless version

$$\tilde{R}\ddot{\tilde{R}} + \frac{3}{2}\dot{\tilde{R}}^2 + \frac{2}{We\tilde{R}} + 4\frac{\dot{\tilde{R}}}{Re\tilde{R}} - \tilde{\Delta} = 0, \tag{H6a}$$

$$\frac{d\tilde{\Delta}}{d\tilde{t}} = \frac{3}{Eu_0} \left(\frac{\partial \tilde{\rho}_V}{\partial \tilde{p}_V} \right)^{-1} \left[-\tilde{\rho}_V \frac{\dot{\tilde{R}}}{\tilde{R}} - \Pi \frac{\tilde{\Theta}}{\tilde{R}} \right], \tag{H6b}$$

R. Ezeta and others

$$\tilde{\Delta} = -\frac{1}{\pi} \int_{\tilde{s}=0}^{\tilde{t}} \frac{\tilde{R}(\tilde{s})^2 \tilde{\Theta}}{\sqrt{\int_{\tilde{w}=\tilde{s}}^{\tilde{t}} \tilde{R}(\tilde{w})^4 d\tilde{w}}} d\tilde{s}, \quad (\text{H6c})$$

$$\tilde{R}(0) = 1, \quad \dot{\tilde{R}}(0) = -1, \quad \tilde{\Delta}(0) = \kappa, \quad (\text{H6d})$$

which are similar to the axisymmetric version. The most important conclusion is that in all cases the value of the parameter Π in (4.14) determines the qualitative behaviour of the vapour pocket, where for $\Pi \gg 1$, a vapour pocket collapse combined with large pressures is expected and, for $\Pi \ll 1$, damped oscillations are seen at much more moderate pressures.

At this point it is maybe good to stress that the axisymmetric version holds unchanged for a full cylindrical bubble such as a torus (although it was derived for a hemicylindrical one), and that boundary conditions may be different from those used in the main text of this paper. For instance, one might want to look at the motion of a bubble that is immersed in a liquid at the vapour pressure, where the bubble wall by some process has obtained a finite (inward) velocity $-V_0$. One then may just use the equations as they were derived in this work, but with $V_{wave} = 0$ in the initial condition, leading to $\kappa = (V_{wave}/V_0)^2 = 0$ in the dimensionless version.

At the other extreme one may think of a quiescent bubble being pressurised at an overpressure Δp_0 . In that case, since $\dot{R}(0) = 0$, one needs to derive a velocity scale from Δp_0 as $V_0 = \sqrt{\Delta p_0/\rho_L}$, which can subsequently be used for the non-dimensionalisation leading to the exact same equations, but with slightly different boundary conditions $\tilde{R}(0) = 1$, $\dot{\tilde{R}}(0) = 0$ and $\tilde{\Delta}(0) = 1$ (or $R(0) = R_0$, $\dot{R}(0) = 0$ and $p_V(0) = p_{V,0} + \Delta p_0$ in the dimensional case).

REFERENCES

- ABRATE, S. 2013 Hull slamming. *Appl. Mech. Rev.* **64** (6), 060803.
- ANCELLIN, M., GHIDAGLIA, J.M. & BROSSET, L. 2012 Influence of phase transition on sloshing impact pressures described by a generalized Bagnold's model. In *Proceedings of the 22nd International Offshore and Polar Engineering Conference (ISOPE), Rhodes, Greece, June 17-22, 2012*, vol. 3, pp. 53–61. International Society of Offshore and Polar Engineers (ISOPE).
- BERGAMASCO, L. & FUSTER, D. 2017 Oscillation regimes of gas/vapor bubbles. *Intl J. Heat Mass Transfer* **112**, 72–80.
- BERGMANN, R., VAN DER MEER, D., STIJNMAN, M., SANDTKE, M., PROSPERETTI, A. & LOHSE, D. 2006 Giant bubble pinch-off. *Phys. Rev. Lett.* **96** (15), 154505.
- BOGAERT, H., LÉONARD, S., BROSSET, L. & KAMINSKI, M.L. 2010 Sloshing and scaling: results from the sloshel project. In *The Twentieth International Offshore and Polar Engineering Conference*, pp. I-10-030. International Society of Offshore and Polar Engineers.
- BRAEUNIG, J.P., BROSSET, L., DIAS, F. & GHIDAGLIA, J.M. 2010 On the effect of phase transition on impact pressures due to sloshing. In *Proceedings of the 20th International Offshore and Polar Engineering Confering (ISOPE), Beijing, China, June 20-25, 2010*, vol. 3, pp. 53–61. International Society of Offshore and Polar Engineers (ISOPE).
- BREDMOSE, H., BULLOCK, G.N. & HOGG, A.J. 2015 Violent breaking wave impacts. Part 3. Effects of scale and aeration. *J. Fluid Mech.* **765**, 82–113.
- BREDMOSE, H., PEREGRINE, D.H. & BULLOCK, G.N. 2009 Violent breaking wave impacts. Part 2: modelling the effect of air. *J. Fluid Mech.* **641**, 389–430.
- BRENNEN, C.E. 2013 *Cavitation and Bubble Dynamics*. Cambridge University Press.
- CALDERÓN-SÁNCHEZ, J., DUQUE, D. & GÓMEZ-GOÑI, J. 2018 Modeling the effect of phase change on LNG impact with open-source CFD. In *Proceedings of the 37th International Conference on Offshore Mechanics and Arctic Engineering (OMAE2018), Madrid, Spain, June 17-22, 2018*, vol. 51203, pp. V001T01A028. ASME-OMAE.
- CHANG, B., CROSON, M., STRAKER, L., GART, S., DOVE, C., GERWIN, J. & JUNG, S. 2016 How seabirds plunge-dive without injuries. *Proc. Natl Acad. Sci. USA* **113** (43), 12006–12011.
- DIAS, F. & GHIDAGLIA, J.M. 2018 Slamming: recent progress in the evaluation of impact pressures. *Annu. Rev. Fluid Mech.* **50** (1), 243–273.

- ERMANYUK, E.V. & OHKUSU, M. 2005 Impact of a disk on shallow water. *J. Fluid Struct.* **20** (3), 345–357.
- EZETA, R., KIMMOUN, L. & BROSSET, L. 2023 Influence of ullage pressure on wave impacts induced by solitary waves in a flume tank. In *Proceedings of the 33rd International Offshore and Polar Engineering Conference (ISOPE), Ottawa, Canada, June 19-23, 2023*, vol. 6, pp. 367–381. International Society of Offshore and Polar Engineers (ISOPE).
- FALTINSEN, O.M. 2000 Hydroelastic slamming. *J. Mar. Sci. Technol.* **5** (2), 49–65.
- FALTINSEN, O.M., LANDRINI, M. & GRECO, M. 2004 Slamming in marine applications. *J. Engng Maths* **48** (3-4), 187–217.
- FALTINSEN, O.M. & TIMOKHA, A.N. 2009 *Sloshing*. Cambridge University Press.
- GRIMSHAW, R. 1971 The solitary wave in water of variable depth. Part 2. *J. Fluid Mech.* **46** (3), 611–622.
- GUIZIEN, K. & BARTHÉLEMY, E. 2002 Accuracy of solitary wave generation by a piston wave maker. *J. Hydraul. Res.* **40** (3), 321–331.
- HATTORI, M., ARAMI, A. & YUI, T. 1994 Wave impact pressure on vertical walls under breaking waves of various types. *Coast. Eng.* **22** (1-2), 79–114.
- HICKS, P.D., ERMANYUK, E.V., GAVRILOV, N.V. & PURVIS, R. 2012 Air trapping at impact of a rigid sphere onto a liquid. *J. Fluid Mech.* **695**, 310–320.
- HOFLAND, B., KAMINSKI, M.L. & WOLTERS, G. 2010 Large scale wave impacts on a vertical wall. *Coast. Eng. Proc.* **32**, 1–15.
- ILINSKII, Y.A., ZABOLOTSKAYA, E.A., HAY, T.A. & HAMILTON, M.F. 2012 Models of cylindrical bubble pulsation. *J. Acoust. Soc. Am.* **132** (3), 1346–1357.
- KAPSENBERG, G.K. 2011 Slamming of ships: where are we now? *Phil. Trans. R. Soc. Lond. A: Math. Phys. Eng. Sci.* **369** (1947), 2892–2919.
- KOROBKIN, A.A. 2004 Analytical models of water impact. *Eur. J. Appl. Math.* **15** (6), 821–838.
- LAFEBER, W., BOGAERT, H. & BROSSET, L. 2012 Elementary loading processes (ELP) involved in breaking wave impacts: findings from the sloshel project. In *ISOPE International Ocean and Polar Engineering Conference*, pp. ISOPEI–I. ISOPE.
- LESSER, M.B. 1981 Analytic solution of liquid-drop impact problems. *Proc. R. Soc. Lond. A: Math. Phys. Sci.* **377**, 289–308.
- LUGNI, C., BROCCINI, M. & FALTINSEN, O.M. 2006 Wave impact loads: the role of the flip-through. *Phys. Fluids* **18** (12), 122101.
- MA, Z.H., CAUSON, D.M., QIAN, L., MINGHAM, C.G., MAI, T., GREAVES, D. & RABY, A. 2016 Pure and aerated water entry of a flat plate. *Phys. Fluids* **28** (1), 016104.
- NOVAKOVIĆ, V., COSTAS, J.J., SCHREIER, S., KIMMOUN, O., FERNANDES, A., EZETA, R., BIRVALSKI, M. & BOGAERT, H. 2020 Repeatability in the new multiphase wave lab (MWL). In *Proceedings of the 30th International Offshore and Polar Engineering Conference (ISOPE), Shanghai, China, October 11–16, 2020*, vol. 3, pp. 2511–2520. International Society of Offshore and Polar Engineers (ISOPE).
- PEREGRINE, D.H. 2003 Water-wave impact on walls. *Annu. Rev. Fluid Mech.* **35** (1), 23–43.
- PEREGRINE, D.H. & THAIS, L. 1996 The effect of entrained air in violent water wave impacts. *J. Fluid Mech.* **325**, 377–397.
- PETERS, A., LANTERMANN, U. & EL MOCTAR, O. 2018 Numerical prediction of cavitation erosion on a ship propeller in model- and full-scale. *Wear* **408**, 1–12.
- PLESSET, M.S. & PROSPERETTI, A. 1977 Bubble dynamics and cavitation. *Annu. Rev. Fluid Mech.* **9** (1), 145–185.
- PLESSET, M.S. & ZWICK, S.A. 1952 A nonsteady heat diffusion problem with spherical symmetry. *J. Appl. Phys.* **23** (1), 95–98.
- PROSPERETTI, A. 2017 Vapor bubbles. *Annu. Rev. Fluid Mech.* **49** (1), 221–248.
- PROSPERETTI, A. & PLESSET, M.S. 1978 Vapour-bubble growth in a superheated liquid. *J. Fluid Mech.* **85** (2), 349–368.
- REUTER, F., DEITER, C. & OHL, C.-D. 2022 Cavitation erosion by shockwave self-focusing of a single bubble. *Ultrason. Sonochem.* **90**, 106131.
- SEDDON, C.M. & MOATAMEDI, M. 2006 Review of water entry with applications to aerospace structures. *Intl J. Impact Eng.* **32** (7), 1045–1067.
- SMITH, N.J., STANSBY, P.K. & WRIGHT, J.R. 1998 The slam force on a flat plate in free flight due to impact on a wave crest. *J. Fluid Struct.* **12** (2), 183–196.
- TRUSCOTT, T.T., EPPS, B.P. & BELDEN, J. 2014 Water entry of projectiles. *Annu. Rev. Fluid Mech.* **46** (1), 355–378.
- WAGNER, H. 1932 Über stoß- und gleitvorgänge an der oberfläche von flüssigkeiten. *Z. Angew. Math. Mech.* **12** (4), 193–215.
- WOOD, D.J., PEREGRINE, D.H. & BRUCE, T. 2000 Wave impact on a wall using pressure-impulse theory. I. Trapped air. *J. Waterway Port Coastal Ocean Eng.* **126** (4), 182–190.